MID-AMERICA TRANSPORTATION CENTER

Report # MATC-MS&T: 126-1

Final Report

WBS: 25-1121-0005-126-1

Condition Evaluation of Precast post-tensioned Concrete Girder Bridges During Fires from Distributed Fiber Optic Sensors

Genda Chen, PhD
Professor and Robert W. Abbett Distinguished Chair in Civil Engineering
Director, Center for Intelligent Infrastructure
Director, INSPIRE University Transportation Center
Associate Director, Mid-America Transportation Center
Department of Civil, Architectural, and Environmental Engineering
Missouri University of Science and Technology

Yanping Zhu, PhD,
Postdoctoral Scholar
Department of Civil, Architectural, and
Environmental Engineering
Missouri University of Science and Technology

2023

A Cooperative Research Project sponsored by
U.S. Department of Transportation- Office of the Assistant Secretary for Research and Technology

The contents of this report reflect the views of the authors, who are responsible for the facts and the accuracy of the information presented herein. This document is disseminated in the interest of information exchange. The report is funded, partially or entirely, by a grant from the U.S. Department of Transportation's University Transportation Centers Program. However, the U.S. Government assumes no liability for the contents or use thereof.

Condition Evaluation of Precast Post-tensioned Concrete Girder Bridges During Fires from Distributed Fiber Optic Sensors

Yanping Zhu, Ph.D. Postdoctoral Fellow
Center for Intelligent Infrastructure
Department of Civil, Architectural, and Environmental Engineering
Missouri University of Science and Technology

Genda Chen, Ph.D., P.E., F. ASCE
Professor and Robert W. Abbett Distinguished Chair in Civil Engineering
Director, Center for Intelligent Infrastructure
Director, INSPIRE University Transportation Center
Associate Director, Mid-America Transportation Center
Department of Civil, Architectural, and Environmental Engineering
Missouri University of Science and Technology

A Report on Research Sponsored by

Mid-America Transportation Center

University of Nebraska–Lincoln

July 2023

Technical Report Documentation Page

1. Report No. 25-1121-0005-126-1	2. Government Accession No.	3. Recipient's Catalog No.
4. Title and Subtitle Condition Evaluation of Precast post-tensioned Concrete Girder Bridges During Fires from Distributed Fiber Optic Sensors		5. Report Date July 2023
		6. Performing Organization Code
7. Author(s) Yanping Zhu, and Genda Chen		8. Performing Organization Report No. 25-1121-0005-126-1
9. Performing Organization Name and Address Center for Intelligent Infrastructure Missouri University of Science and Technology 500 W. 16th Street Rolla, MO 65409-0810		10. Work Unit No. (TRAIS)
		11. Contract or Grant No. 69A3551747107
12. Sponsoring Agency Name and Address Mid-America Transportation Center 2200 Vine St PO Box 830851 Lincoln, NE 68583-0851		13. Type of Report and Period Covered Final Report January 1, 2021 - December 31, 2023
		14. Sponsoring Agency Code MATC TRB RiP No. 91994-84
15. Supplementary Notes		

16. Abstract

This report summarizes the results and findings of Mid-America Transportation Research Center (MATC) research project No. 65575. It is focused on the measurement of strain and temperature in concrete and prestressed structures at ambient or high temperature using a pulse pre-pump Brillouin optical time domain analysis (PPP-BOTDA) technique. The main objectives of this study are: (a) to experimentally characterize the effects of multilayered coatings on the performance of distributed fiber optic sensors (DFOS) when the coatings experience softening and melting at high temperatures; (b) to develop a spiral deployment scheme of DFOS and monitor/assess the post-tensioned force in 7-wire twisted steel cables based on PPP-BOTDA. The Y-DFOS was found to no longer be strain-free at high temperatures since the softened sheath, aramid yarns, buffer, and polymer coatings became viscous and adhered to the surrounding mortar above softening temperatures, i.e., 263-320 ℃. Both the B-DFOS and W-DFOS captured uneven strain distributions along the mortar specimen due to nonuniform temperature distribution, mortar heterogeneity, and strain transfer efficiency. The maximum, minimum, and average cable forces integrated from the measured strain data were compared and validated with those from a load cell. The maximum (or average) cable force was linearly related to the ground truth data with a less than 10% error between them after any initial slack had been removed from the test setup. The post-tensioned force loss was bounded by approximately 30% using the test setup designed in this study.

17. ORCID No. of each Researcher Genda Chen: 0000-0002-0658-4356	18. Distribution Statement		
19. Security Classif. (of this report) Unclassified	20. Security Classif. (of this page) Unclassified	21. No. of Pages 87	22. Price

Table of Contents

Acknowledgments vii
Disclaimer viii
Abstract ix
Chapter 1 Effect of the Multilayered Coating of Single-mode Optical Fibers on Distributed Temperature and Strain Measurement in Mortar Specimens 1
1.1 Introduction 1
1.2 Experimental Program 5
1.2.1 Distributed Fiber Optic Sensor (DFOS) 5
1.2.2 Soften and Melt Temperature Characterization 6
1.2.3 Mortar and Specimen Preparation 8
1.2.4 Test Setup and Instrumentation 9
1.3 Analytical Calculation 11
1.3.1 Temperature and Strain Calibration Calculation 12
1.3.2 Thermal Displacement Calculation 13
1.4 Results and Discussion 14
1.4.1 Soften and Melt Temperatures of Multilayered Coatings 14
1.4.2 Calibration Results of DFOS 18
1.4.3 Temperature Distribution along the Length of Mortar Specimen 23
1.4.4 Strain Distribution along the Length of Mortar Specimen 26
1.4.5 Free-expanded Thermal Displacement of the Cantilevered Mortar Specimen 33
1.5 Summary 35
Chapter 2 Spiral Deployment of Optical Fiber Sensors for Distributed Strain Measurement in Seven-Wire Twisted Steel Cables, Post-Tensioned against Precast Concrete Bars 38
2.1 Introduction 38
2.2 Experimental Program 41
2.2.1 Material properties 41
2.2.2 Specimen design and preparation 44
2.2.3 Distributed fiber optic sensing principle 46
2.2.4 Instrumentation and loading 48
2.3 Results and Discussion 53
2.3.1 Cable force during tensioning process 53
2.3.2 Linear regression analysis 74
2.3.3 Instant prestress loss 77
2.4 Summary 79
Chapter 3 Conclusions 81
References 83

List of Figures

Figure 1.1 Distributed fiber optic sensor (DFOS) with multilayered coatings 6
Figure 1.2 Test setup and instrumentation 10
Figure 1.3 PPP-BOTDA operation principle (Bao and Chen 2015) 12
Figure 1.4 Segments of a DFOS under combined tension and temperature effects 13
Figure 1.5 Representative distribution of temperature and strain along the test specimen 14
Figure 1.6 Determination of the melt onset temperature of the W-DFOS coatings 15
Figure 1.7 Finite element model for optical fiber 17
Figure 1.8 Temperature calibration of one type of temperature sensor: Y-DFOS 19
Figure 1.9 Temperature calibration of two types of strain sensors 20
Figure 1.10 Strain calibration of the W-DFOS strain sensor 22
Figure 1.11 B-DFOS strain coefficient versus temperature relationship 23
Figure 1.12 Temperature distribution measured along the length of a mortar specimen 24
Figure 1.13 Change in maximum temperatures over time 26
Figure 1.14 Longitudinal distribution of axial strains measured by E-W-DFOS 27
Figure 1.15 Longitudinal distribution of strains measured from S-W-DFOS 29
Figure 1.16 Longitudinal distribution of strains measured from E-B-DFOS 30
Figure 1.17 Longitudinal distribution of strains measured from S-B-DFOS 31
Figure 1.18 The DFOS measured strain versus the calculated thermal-induced strain at the mid-length of the mortar specimen 33
Figure 1.19 Thermal-induced deformation measured from various DFOS installations 35
Figure 2.1 (a) Fiber appearance and fiber length of 50 mm; (b) Concrete mixture in a mixer with a capacity of 170 L; (c) Compressive test for cylinder concrete specimen. 42
Figure 2.2 Specimen fabrication: (a) mold assembly; (b) plastic pipe and corrugated steel duct for post-tensioning strand and grouting; (c) casting specimens. 45
Figure 2.3 PPP-BOTDA working principle. 48
Figure 2.4 (a) Distributed fiber optic sensors instrumentation on the steel strand; (b) DFOS taken out from the reserved holes; (c) cross-section of a steel strand with optical fibers. 50
Figure 2.5 (a) New tensioning frame and (b) overall test setup 53
Figure 2.6 Strain relationship and lay angle (Moon et al. 2010). 55
Figure 2.7 (a) Calibrated load cell readings for PC1; strain distribution along the strand (b) one strain fiber (W1); (c) the other fiber (W); (d) applied force changes at different load steps. 58
Figure 2.8 (a) Load cell readings for PC5; (b) strain distribution along the strand (W1and W fibers) (In the legend, the first number represents the load step, and the second number represents measurement times at the load step); (c) applied force changes at different load steps 61
Figure 2.9 (a) Load cell readings for PC6; (b) strain distribution along the strand (W1and W fibers) (In the legend, the first number represents the load step, and the second number represents measurement times at the load step); (c) applied force changes at different load steps 63
Figure 2.10 (a) Load cell readings for PC2; (b) strain distribution along the strand (W1and W fibers) (In the legend, the first number represents the load step, and the second number represents measurement times at the load step); (c) applied force changes at different load steps 65

Figure 2.11 (a) Load cell readings for PC3-1; (b) strain distribution along the strand (W1and W fibers) (In the legend, the first number represents the load step, and the second number represents measurement times at the load step); (c) applied force changes at different load steps..... 67
Figure 2.12 (a) Load cell readings for PC3-2; (b) strain distribution along the strand (W1and W fibers) (In the legend, the first number represents the load step, and the second number represents measurement times at the load step); (c) applied force changes at different load steps..... 69
Figure 2.13 (a) Load cell readings for PC4-1; (b) strain distribution along the strand (W1and W fibers) (In the legend, the first number represents the load step, and the second number represents measurement times at the load step); (c) applied force changes at different load steps..... 71
Figure 2.14 (a) Load cell readings for PC4-2; (b) strain distribution along the strand (W1and W fibers) (In the legend, the first number represents the load step, and the second number represents measurement times at the load step); (c) applied force changes at different load steps..... 73
Figure 2.15 (a) Prestressing force versus DFOS average strain; (b) prestressing force versus DFOS average strain calculated force..... 75
Figure 2.16 (a) Prestressing force versus DFOS max strain; (b) prestressing force versus DFOS max strain calculated force. 76
Figure 2.17 (a) Prestressing force versus DFOS min strain; (b) prestressing force versus DFOS min strain calculated force. 77
Figure 2.18 Prestress loss percentage for all specimens in the present test setup. 78

List of Tables

Table 1.1 Characteristics of III Portland cement and Missouri river sand 9
Table 1.2 Summary of characteristic temperatures from TGA-DSC tests (roundoff to integer) . 18
Table 2.1 Mix proportions of concrete 43
Table 2.2 Fiber properties 44
Table 2.3 Specimen design with different parameters 46
Table 2.4 Prestressing force monitored by load cell and DFOS for PC1 (unit: kN). 59
Table 2.5 Prestressing force monitored by load cell and DFOS for PC5 (unit: kN). 62
Table 2.6 Prestressing force monitored by load cell and DFOS for PC6 (unit: kN). 64
Table 2.7 Prestressing force monitored by load cell and DFOS for PC2 (unit: kN). 66
Table 2.8 Prestressing force monitored by load cell and DFOS for PC3-1 (unit: kN). 68
Table 2.9 Prestressing force monitored by load cell and DFOS for PC3-2 (unit: kN). 70
Table 2.10 Prestressing force monitored by load cell and DFOS for PC4-1 (unit: kN). 72
Table 2.11 Prestressing force monitored by load cell and DFOS for PC4-2 (unit: kN). 74

Acknowledgments

Financial support was provided by Mid-America Transportation Center under contract agreement No. 65575. Thanks are due to technicians Jeffrey Heniff, Ronald Leckrone, and John Whitchurch in Structural Highbay Lab, Missouri S&T, for their assistance during preparation and early tests of the samples.

Disclaimer

The contents of this report reflect the views of the authors, who are responsible for the facts and the accuracy of the information presented herein. This document is disseminated in the interest of information exchange. The report is funded, partially or entirely, by a grant from the U.S. Department of Transportation's University Transportation Centers Program. However, the U.S. Government assumes no liability for the contents or use thereof.

Abstract

This report summarizes the results and findings of the Mid-America Transportation Center (MATC) research project No. 65575. It is focused on the measurement of strain and temperature in concrete and prestressed structures at ambient or high temperature using a pulse pre-pump Brillouin optical time domain analysis (PPP-BOTDA) technique. The main objectives of this study are: (a) to experimentally characterize the effects of multilayered coatings on the performance of distributed fiber optic sensors (DFOS) when the coatings experience softening and melting at high temperatures; (b) to develop a spiral deployment scheme of DFOS and monitor/assess the post-tensioned force in 7-wire twisted steel cables based on PPP-BOTDA. The Y-DFOS was found to no longer be strain-free at high temperatures since the softened sheath, aramid yarns, buffer, and polymer coatings became viscous and adhered to the surrounding mortar above softening temperatures, i.e., 263-320 ℃. Both the B-DFOS and W-DFOS captured uneven strain distributions along the mortar specimen due to nonuniform temperature distribution, mortar heterogeneity, and strain transfer efficiency. The W-DFOS showed higher measured strains than the calculated thermal-induced strains at 100-300 ℃ due to the high thermal expansion coefficient of the additional buffer. The B-DFOS gave smaller measured strains than the thermal-induced strains at 300-500 ℃.

Eight concrete bar specimens were cast, each with a pre-embedded plastic or metal duct at its center and post-tensioned by a steel strand through the duct once instrumented with two strain and two temperature sensors. Each DFOS was placed in a spiral shape between two surface wires of a steel cable and glued to the steel cable by epoxy. The strand was loaded/unloaded and monitored by measuring the Brillouin frequency shifts and correlating them with the applied strains and resulting cable force after temperature compensation. The maximum,

minimum, and average cable forces integrated from the measured strain data were compared and validated with those from a load cell. The maximum (or average) cable force was linearly related to the ground truth data with a less than 10% error between them after any initial slack had been removed from the test setup. The post-tensioned force loss was bounded by approximately 30% using the test setup designed in this study.

Chapter 1 Effect of the Multilayered Coating of Single-mode Optical Fibers on Distributed Temperature and Strain Measurement in Mortar Specimens

1.1 Introduction

The displacement of cement, mortar, and concrete at elevated temperatures warrants further studies on the performance and safety evaluation of concrete/masonry buildings subjected to fires (Kodur et al. 2020, Lee et al. 2016, Gawin et al. 2004). Like thermal conductivity, specific heat, and mass loss, thermal deformation in concrete and masonry structures is a temperature-dependent property of materials. These thermal properties determine the temperature rise and distribution in structures, potentially inducing degradation of the structures due to the physiochemical change of materials (Sabeur and Colina 2015). The thermal deformation could be indicative of potential damage and behavior in concrete structures. It is thus critically important to measure the thermal deformation, which has been historically challenging in fire engineering.

Different deformation measurement methods have been developed in the literature. The most used tool is a linear position transducer called Linear Variable Differential Transformer (LVDT) (Lee et al. 2016, Le et al. 2017, and Le et al. 2019). The LVDT is usually placed out of the heat region and needs a displacement transfer bar made of quartz. As a result, the LVDT can only provide an average strain over the heat length. The second method is an extensometer placed inside the heat region. The capacity of the extensometer is often limited in fire engineering. Its function cannot be guaranteed particularly under combined thermal and mechanical loading. The third method is a high temperature strain gauge. The inherent measurement performance and the bond between the strain gauge and its substrate (i.e., concrete or steel) directly affect the accuracy of measured deformation at high temperature. The above three methods are all in direct contact with the substrate. Different from the contact methods is a

non-contact method with a laser sensor, which measures deformation between two discrete points. However, the infrared beams are easily disturbed by thermal radiation and the alternative blue laser diodes are costly. Another non-contact method is a digital image correlation (DIC) method (Pan et al. 2020, Novak and Zok 2011). The main challenges for the DIC technology include (1) the camera placed outside the heat region looking into the test specimen though small windows on the heating facility; (2) the measured data influenced by hot air circulation, smoke, and soot particles from concrete burning; and (3) the inconsistency of lighting conditions. Other innovative methods for measuring the thermal expansion (Loser et al. 2010, Tang et al. 2020) include a volume-based technique and a coupled shrinkage and temperature induced expansion effect.

Distributed fiber optic sensors (DFOS) have recently been used for strain and temperature measurements in civil structures based on the Principles of Raman, Rayleigh, and Brillouin scattering. Of particular interest is a pulse pre-pump Brillouin optical time domain analysis (PPP-BOTDA) that can provide desirable accuracy and precision for distributed strain and temperature measurements. The commercialized PPP-BOTDA technology has a spatial resolution of 2 cm over a measurement length of 500 m. This technology has been applied to measure strain distributions and detect cracks at ambient temperatures (Bao et al. 2016, Bao and Chen 2015, Bao et al. 2017). Moreover, Bao and Chen (2016a) calibrated a DFOS for its temperature coefficient under no mechanical strain and for its strain coefficient under preset temperatures. Annealing can extend the operation temperature of the DFOS to 1000 ℃ when free of mechanical strain (Bao and Chen 2016b). Note that these calibration tests were limited to the use of bare optical fibers with a glass core (8.2 μm) and a cladding layer (125 μm). Various DFOS systems have been applied to concrete beams (Bao et al. 2017a), steel beams (Bao et al. 2017b),

and steel-concrete composite slabs (Bao et al. 2020, Zhu et al. 2021) to measure spatially distributed temperatures. Bao et al. (2017a, 2020) assumed that the optical fiber with a sheath layer could move freely inside the sheath at elevated temperatures, which has not been validated when the fiber was embedded in concrete. Although the strains in steel beams under fire conditions were locally measured by a customized DFOS that is locally attached to the beams through glass tubes (Bao and Chen 2016a, Bao et al. 2017b), this customized sensor provided a point strain over a length of 50 mm. Moreover, the strain transfer through high temperature adhesive was not well understood and fully validated in steel structures. Additionally, the strain transfer mechanism from a concrete structure to an embedded DFOS with coatings over distance under high temperatures requires further understanding.

At an ambient temperature, the strain has been successfully measured with a DFOS by considering the strain transfer in adhesive and protective layers between the optical fiber and the host material (Tan 2021). The transfer of these interfacial stresses leads to a stress lag on the optical fiber. At high temperatures, however, the strain transfer mechanism and efficiency may depend upon the application temperature due to temperature-dependent material properties of the adhesive and protective layers. Yang et al. (2021) provided a theoretical solution for the thermal-induced strain measurement using the DFOS with an interlayer under uniform and gradient temperature loading cases. Temperature-dependent material properties (i.e., Young's modulus and thermal expansion coefficient) of the matrix, protective layer, and glass core as well as the geometrical parameters of the optical fiber were taken into account. Note that the thermal expansion coefficient of the glass core was assumed to be approximately zero. The theoretical solution was not verified and validated by experimental tests. Wang and Dai (2019) measured the thermal deformations of alumina and polypropylene plates with surface bonded fiber Bragg

grating sensors subjected to 30-70℃. The multiple contacted layers (i.e., host material, protective layer, adhesive layer, and optical fiber) affected the thermal deformation transfer.

As mentioned above, Brillouin scattering based fiber optic sensors have recently proved promising for distributed temperature and strain measurement, which is critically important in condition assessment of large-scale reinforced concrete structures under fires. Their measurement performance, however, largely depends on the temperature-dependent behavior of multilayer coating on a single-mode optical fiber. The recent study based on Rayleigh scattering, which is several times more sensitive to temperature and strain changes than Brillouin scattering, clearly indicated a significant effect of coating softening and melting on strain and temperature measurement along the surface of a rectangular steel bar (Zhu and Chen 2022). It was thus insufficient to fully understand the coating effect on high temperature measurement in terms of Rayleigh vs. Brillouin scattering measurement accuracy, surface-attached vs. embedded sensor confinement, and steel vs. mortar thermal conductivity (thus maximum application temperature). In addition, a protective tight buffet on single-mode optical fibers may be selected for civil engineering applications in harsh construction environments, which was not included in the previous study (Zhu and Chen 2022).

The main objective of this study is to experimentally characterize the effects of multi-layer coating on the performance of a DFOS as the coating experiences softening and melting. This study used multiple DFOS systems to measure temperature and strain distributions as well as resulting free displacement of mortar subjected to 20-500℃ in temperature. Several types of DFOS systems are calibrated when bonded on the surface of a mortar specimen with a high temperature adhesive or embedded along the centerline of the mortar specimen during casting. Unlike thermocouples, the DFOS can be used to measure a non-uniform temperature distribution

in a relatively short region (i.e., inside a high temperature furnace). The temperature distribution can be used to compensate for the strains measured along the length of optical fiber. The strains measured from the DFOS are compared with those calculated from the thermal expansion coefficient at different temperatures and the distributed strain along the DFOS is integrated to obtain the measured free-end displacement at each temperature for regression analysis.

1.2 Experimental Program

1.2.1 Distributed Fiber Optic Sensor (DFOS)

Figure 1.1(a) shows three types of distributed sensors made of single-mode optical fibers with different coatings: B-DFOS, W-DFOS, and Y-DFOS. The B-DFOS has a soft (inner) layer of coating and a stiff (outer) layer of coating. The Y-DFOS has a soft (inner) layer of coating, a stiff (outer) layer of coating, a tight (white) buffer outside the outer coating, aramid yarns, and a sheath layer. The W-DFOS has a soft (inner) layer of coating, a stiff (outer) layer of coating, and a tight (white) buffer outside the outer coating after the sheath layer with aramid yarns as shown in Figure 1.1(b) has been stripped off the Y-DFOS. Each DFOS includes an 8.2-μm-diameter glass core and a 125-μm-diameter glass cladding. The glass cladding ensures that the light is guided through the glass core. Both the core and cladding are made of two types of silica glass with nearly the same material properties so they are subjected to little or no shear strain even at high temperatures. The outer diameters of the inner and outer coatings are 190 μm and 242 μm, respectively. The tight buffer has a diameter of 880 μm. The three layers are used to protect the glass fiber from abrasion, mechanical impact, and environmental exposure, enhance mechanical strength, and reduce signal attenuation due to micro-bending. The three layers are composed of monomers, oligomers, photoinitiators, and additives. They are burned off at 300-400 ℃, while the glass core and cladding can survive above 1000 ℃. The B-DFOS and W-DFOS are used to

measure both strain and temperature while the Y-DFOS is assumed to measure temperature only because the sheath is in direct contact with its surrounding concrete and the optical fiber inside the sheath is free to move inside the sheath as demonstrated at ambient temperature by Bao et al. (2017a). The thermal conductivity of the sheath is 3.0 W/ (m.K), which is larger than that of concrete (smaller than 2.0 W/ (m.K)).

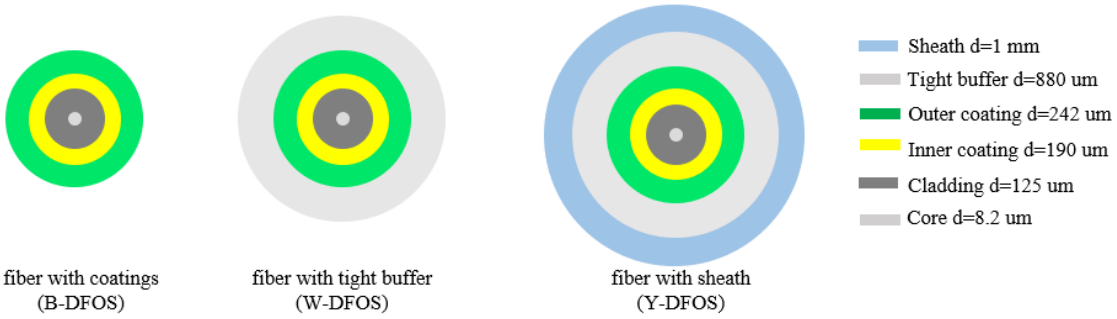

(a) Cross sectional view of three types of sensors (B-DFOS, W-DFOS, and Y-DFOS)

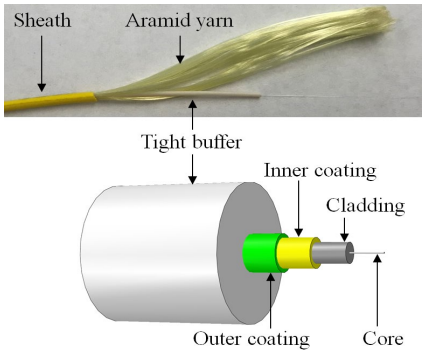

(b) Three-dimensional view and prototype of Y-DFOS

Figure 1.1 Distributed fiber optic sensor (DFOS) with multilayered coatings

1.2.2 Soften and Melt Temperature Characterization

The inner and outer coatings, tight buffer, aramid yarn, and sheath of the silica optical fiber sensors soften and melt at high temperatures. These materials were tested to support

interpretation of the sensor data. The sheath, aramid yarn, and tight buffer materials were cut from a Y-DFOS. Note that the tight buffer material in the W-DFOS is identical to that in the Y-DFOS. Two samples of the inner and outer coatings were prepared using a fiber stripper: B-DFOS coatings and W-DFOS coatings. All samples were tested in the nitrogen gas environment with a flow rate of 100 ml/min and measured from a Simultaneous Thermal Analyzer (SDT, TA Instruments Q600). The samples were heated from ambient temperature to 600 ℃ at a rate of 10 ℃/min.

Differential scanning calorimetry (DSC) was used to investigate the melting process of polymers to heating. Melting is an endothermic process that is accompanied by the absorption of heat. Thus, the heat flow (magnitude) increases locally. The melting temperature can be identified locally with an aid of the Universal Analysis 2000 software (V4.5A) in two quantities: melt peak temperature corresponding to the peak of a heat flow curve and melt onset temperature slightly below the melt peak temperature as determined traditionally by the intersection point between a constant heat flow and the tangential line near the peak temperature as exemplified by Blaine (2022).

The procedure by Blaine (2022) works well for idealized materials with an approximate constant heat flow clearly observed on two sides of a local heat absorption region centered at the melt peak temperature. In this application, the heat flow curves are quite irregular. Thus, a new procedure with no ambiguity is proposed to determine the melt onset temperature:

1. The derivative of each heat flow curve as a function of time or the change in heat flow over time is obtained.
2. The melt peak temperature is determined corresponding to the peak (negative value) of the heat flow curve with a zero-slope point of the heat flow curve (i.e., no change in heat

capacity at that instant) since the zero slope prior to the melt peak temperature is likely associated with the crystallization temperature when the coating releases heat to its surrounding in an exothermic process.

The maximum slope (negative value) on the derivative curve immediately prior to the melt peak temperature is identified. The tangential line at the maximum slope is intercepted by another straight line connecting the zero-slope points immediately before and after the melt peak temperature. The corresponding temperature at the interception is defined as the melt onset temperature.

1.2.3 Mortar and Specimen Preparation

Mortar was prepared with a cement-water ratio of 0.5 and a sand-cement ratio of 2. The used ASTM Type III Portland cement had a Blaine surface area of 562 m2/kg and a specific gravity of 3.15. The used river sand had a specific gravity of 2.65, a diameter of 0-4.75 mm and a water absorption of 0.14%. Other characteristics of the raw materials are referred to in Table 1.1 (Meng et al. 2017). Each mortar specimen prepared in this study was 600 mm long with a cross section of 20 mm × 20 mm. All the specimens were covered with a plastic sheet after casting, demolded after 24 hours, and cured in water at 21 ± 2℃. The specimens were taken out of water to dry for five days prior to instrumentation.

Table 1.1 Characteristics of III Portland cement and Missouri river sand

Ingredients	Type III Portland cement	Missouri river sand
SiO_2 (%)	19.72	80.3
Al_2O_3 (%)	5.10	10.5
Fe_2O_3 (%)	2.76	3.43
CaO (%)	64.50	1.72
MgO (%)	2.30	1.70
SO_3 (%)	3.25	1.07
Na_2O eq. (%)	0.33	-
C_3S (%)	65.23	-
C_2S (%)	7.33	-
C_3A (%)	8.85	-
C_4AF (%)	8.40	-
Loss of ignition (%)	2.60	1.28
Blaine surface area (m^2/kg)	562	-
Specific gravity	3.15	2.65

1.2.4 Test Setup and Instrumentation

Figure 1.2(a) shows the test setup for DFOS strain calibration. One optical fiber was gripped at two ends using protective sleeves to avoid the fractural damage of the optical fiber during mechanical loading. The protective sleeve was originally designed to protect fusion splices of an optical fiber. Inside the sleeve was a steel bar that provided needed strength in the gripped areas. At each end of the furnace, a ceramic fiber blanket was used to block the ends to minimize heat exchange between the heat region in a furnace and its surroundings. With a temperature control system made by Applied Test System, Inc., the temperature inside the furnace was set to 20 ℃, 100 ℃, 200 ℃, 300 ℃, 400 ℃, 500 ℃, 600 ℃, 700 ℃, and 800 ℃. Each target temperature was sustained for 20 min to ensure that the furnace temperature becomes as uniform as possible. After that, the mechanical load was applied using a load frame at a displacement rate of 0.5 mm/min until the brittle fracture failure of the optic fiber. During the tensile testing, the applied load halted at a displacement interval of 1 mm to get the DFOS measured at the target temperatures. The spatially distributed Brillouin frequency spectra were measured along the length of the tested DFOS using a Neubrescope data acquisition system

(Model NBX7020). The preset measurement parameters in the data acquisition system were as follows: 0.2 ns pulse bandwidth, an average account of 2^{15}, 2 cm spatial resolution, 1 cm sampling resolution, and measurement distance of 50 m. The reading time depends on the scanning frequency range and step. The DFOS temperature calibration test setup was the same as that for the DFOS strain calibration except the bottom end of the furnace was free to move without gripping.

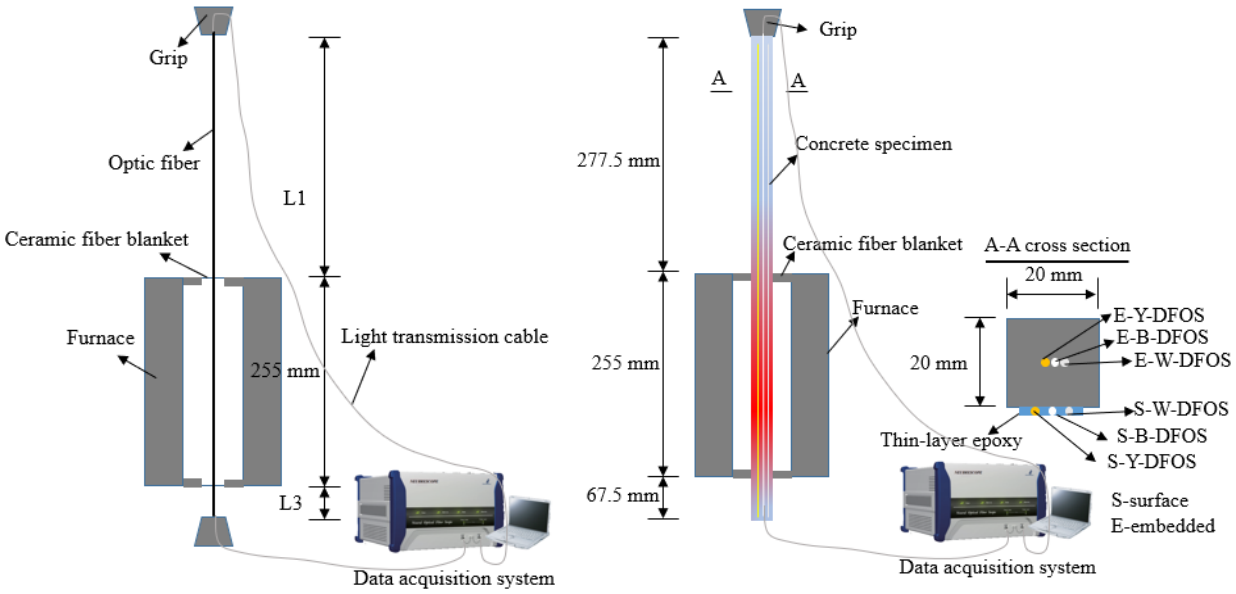

(a) Strain calibration (b) Thermal deformation measurement

Figure 1.2 Test setup and instrumentation

Figure 1.2(b) shows the test setup for mortar free displacement measurement at high temperatures. The bottom end of the mortar specimen was subjected to no mechanical load. The mortar specimen was instrumented with six sensors in two groups: embedded and surface-attached. The three embedded sensors along the centerline of the mortar specimen are designated as E-Y-DFOS, E-W-DFOS, and E-B-DFOS. The three surface-attached sensors are designated as

S-Y-DFOS, S-W-DFOS, and S-B-DFOS, which were covered and adhered to one side of the specimen by a high-temperature adhesive or temperature resistant metallic paste (J-B-WELD made in USA). The adhesive was set in 1 h and cured for 24 h; it can withstand continuous heat up to 538 ℃. It was 1-2 mm thick and 15 mm wide. For strain calculations with the W-DFOS and B-DFOS, the temperature compensation was measured by the Y-DFOS (Bao et al. 2017b).

1.3 Analytical Calculation

PPP-BOTDA stimulates Brillouin scattering (the interaction of light with the acoustic modes of vibration in an optical fiber) by introducing a long-duration pulse before a short-duration pulse arrives. It measures temperature and strain changes from the change in the refractive index of the optical fiber and the speed of acoustic waves traveling along the optical fiber. As shown in Figure 1.3, a forward pump pulse wave and a backward probe continuous wave are sent from two ends of an optical fiber and counter-propagate to cause backscattering at the location of strain and temperature change. Once the frequency difference between the pulse and continuous waves is tuned into the optical fiber Brillouin frequency, Brillouin loss or gain occurs as a function of fiber medium density. The density and refractive index are affected by both strain (ε) and temperature (T), while the Young's modulus and Poisson's ratio are affected by temperature (T) only (Bao and Chen 2016a). Therefore, the strain change ($\Delta\varepsilon$) and temperature change (ΔT) from their reference values (e.g., zero strain and room temperature) used during calibration tests cause a shift in the Brillouin frequency of the optical fiber sensor. The Brillouin frequency shift ($\Delta\nu_B$) can be expressed as:

$$\Delta\nu_B = C_\varepsilon \Delta\varepsilon + C_T \Delta T \tag{1.1}$$

where C_ε and C_T represent the strain and temperature sensitivity coefficients, respectively.

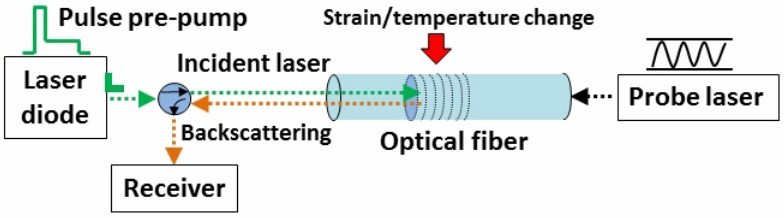

Figure 1.3 PPP-BOTDA operation principle (Bao and Chen 2015)

1.3.1 Temperature and Strain Calibration Calculation

According to equation (1.1), the temperature calibration coefficients for the Y-DFOS, W-DFOS, and B-DFOS can be determined from $\Delta\nu_B = C_T\Delta T$ when the sensor is free from straining effects. For the strain calibration coefficients of the W-DFOS and B-DFOS under different temperatures, the effect of temperature distribution over the length of a distributed strain sensor is taken into account. The temperature inside a furnace reaches to its maximum at the mid-height of the furnace and linearly reduces towards the two ends of the furnace as observed from the previous study (Bao et al. 2017b) and from Section 1.4 of this study. However, since the thermal expansion is linearly proportional to the temperature change, the bi-linear temperature distribution inside the furnace is simplified and represented by an average temperature (constant). The temperature in the optical fiber outside the furnace is equal to the room temperature. As shown in Figure 1.4 for a typical distributed strain sensor, the elongation ΔL_2 in the heated segment L_2 of the optical fiber can be calculated by equations (1.2)-(1.3) using the total elongation (ΔL) recorded by the load frame.

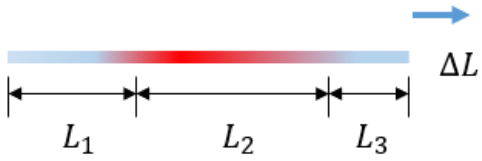

Figure 1.4 Segments of a DFOS under combined tension and temperature effects

$$\Delta L = \Delta L_1 + \Delta L_2 + \Delta L_3 \tag{1.2}$$

$$\Delta L_1 = (\frac{\Delta V_{B1}}{\alpha}) \times L_1 \text{ and } \Delta L_3 = (\frac{\Delta V_{B3}}{\alpha}) \times L_3 \tag{1.3}$$

where ΔV_{B1} and ΔV_{B3} are the average Brillouin frequency shifts in cold L_1 and L_3 segments, respectively; α is the strain sensitivity coefficient C_ε of DFOS at the room temperature. The calculated elongation ΔL_2 from equation (1.2) is used to determine the average strain and then the average frequency shift for segment 2 at high temperature following the shift-strain relation.

1.3.2 Thermal Displacement Calculation

Figure 1.5 shows a general temperature distribution and strain distribution along a mortar specimen. The thermal displacement (Δl) can be calculated by the following equation:

$$\Delta l = \int \varepsilon\,(T)dx = \int \Delta v\,(\varepsilon)/C_\varepsilon(T)dx = \int\big(\Delta v - \Delta v\,(T)\big)/C_\varepsilon(T)dx \tag{1.4}$$

where $\varepsilon\,(T)$ is the strain at temperature T; $\Delta v\,(\varepsilon)$ is the Brillouin frequency shift caused by strain only; Δv is the Brillouin frequency shift caused by both strain and temperature; and $\Delta v\,(T)$ is the Brillouin frequency shift caused by temperature only, which can be obtained from Y-DFOS.

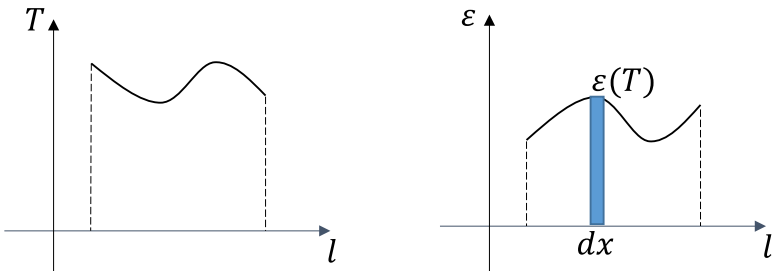

(a) Temperature (b) Strain

Figure 1.5 Representative distribution of temperature and strain along the test specimen

1.4 Results and Discussion

1.4.1 Soften and Melt Temperatures of Multilayered Coatings

Figures 1.6(a) and 1.6(b) present the heat flow curve and its first derivative with respect to time, respectively, from the thermogravimetric analysis of the W-DFOS coatings. The sudden increase (negative value) in heat flow after a flat or concave downward heat flow curve in Figure 1.6(a) is indicative of the melting behavior in multilayer materials (Blaine 2022). Thus, the third zero-slope point in Figure 1.6(b) corresponds to the melt peak temperature, which is 406.62°C. The second and fourth zero-slope points in Figure 1.6(b) take place at 309.28°C and 480.96°C, respectively. The straight line connecting the second and fourth zero-slope points is shown in Figure 1.6(a). The straight line is intercepted by a tangential line at the maximum slope point at the melt onset temperature of 348.91°C according to the proposed procedure in Section 2.2. Note that two decimal points are kept in temperature values to ensure accuracy when identifying the maximum slope and zero slope. In the following analysis, roundoff integers are used in temperature values.

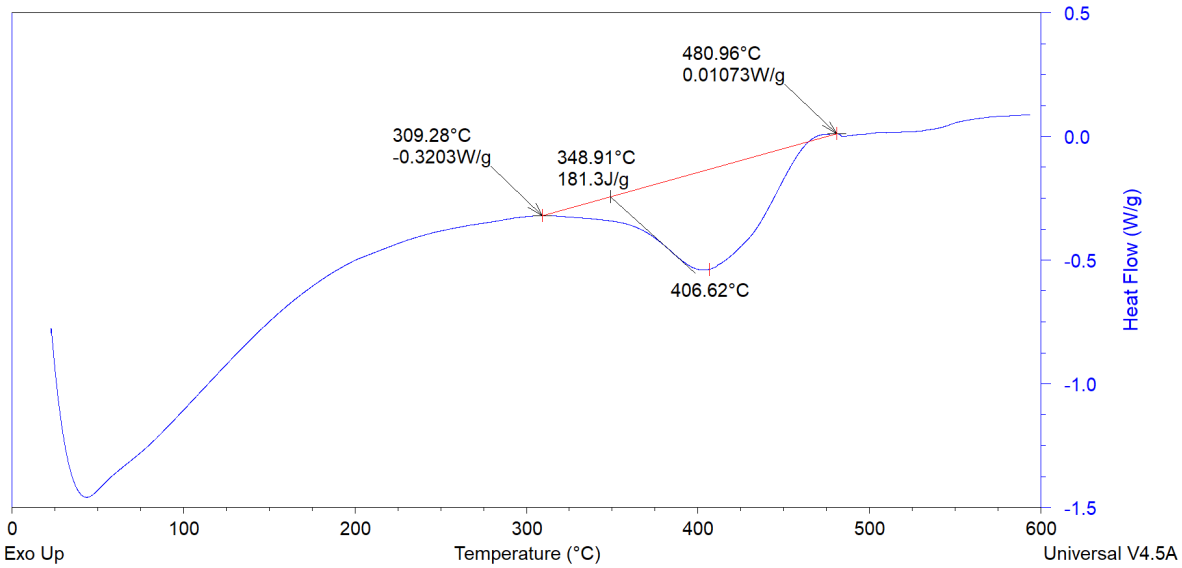

(a) The heat flow curve of the W-DFOS

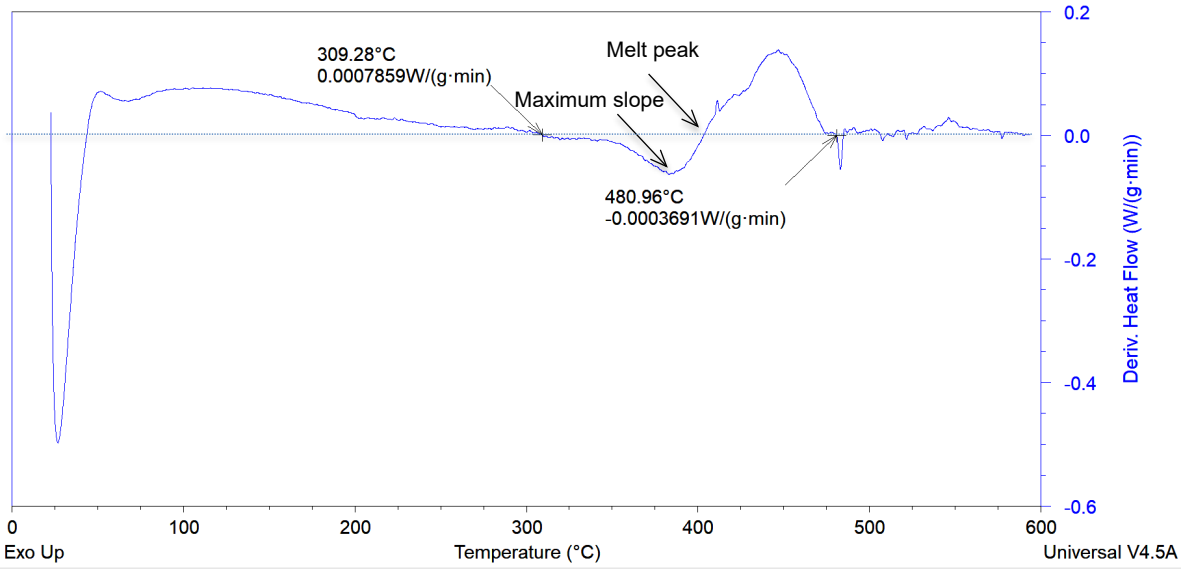

(b) The first derivative of the heat flow curve with time

Figure 1.6 Determination of the melt onset temperature of the W-DFOS coatings

Figure 1.7(a) compares the weight (black lines) and heat flow (red lines) of two types of coatings and Figure 1.7(b) presents the weight and heat flow of the sheath, aramid yarn, and tight buffer. According to the proposed procedure in Section 2.2, the melting onset-peak temperatures

(roundoff to integers) of the B-DFOS and W-DFOS coatings are determined to be 283-315 ℃ and 349-407 ℃ while the melting temperatures of the sheath, aramid yarn, and tight buffer materials are 281-297 ℃, 344-440 ℃, and 280-303 ℃, respectively. The temperatures corresponding to 5% reduction in weight are 282 ℃, 320 ℃, 263 ℃, 276 ℃, and 263 ℃ for the B-DFOS coatings, W-DFOS coatings, tight buffer, aramid yarn, and sheath, respectively, as indicated by the vertical long dash lines in Figure 1.7.

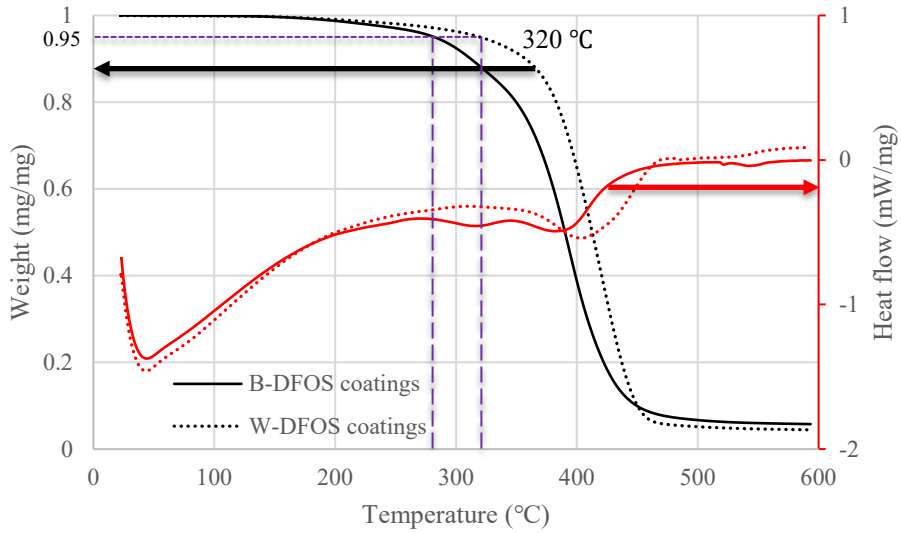

(a) B-DFOS and W-DFOS coatings

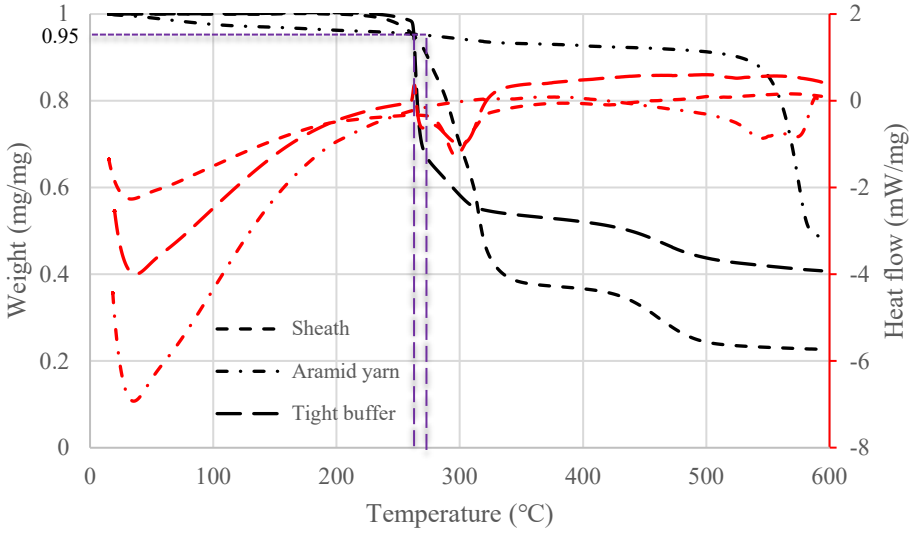

(b) Tight (white) buffer, aramid yarn, and sheath

Figure 1.7 Finite element model for optical fiber

Table 1.2 Summary of characteristic temperatures from TGA-DSC tests (roundoff to integer)

Materials	Softening temperature (℃) corresponding to 5% reduction in weight	Melt onset temperature (℃)	Melt peak temperature (℃)
Sheath	263	281	297
Aramid yarn	276	344	440
Tight buffer	263	280	303
W-DFOS coatings	320	349	407
B-DFOS coatings	282	283	315

1.4.2 Calibration Results of DFOS

Figure 1.8 shows the calibrated results of Y-DFOS. Figure 1.8(a) shows representative measured Brillouin frequencies along the length of Y-DFOS under various applied temperatures. The Brillouin frequency shift from the room temperature condition occurs inside the furnace region only since the Y-DFOS outside the furnace is subject to the room temperature. This observation generally verifies the previous assumption used in analysis. In addition, the two measurements at 1 min and 20 min (e.g., 900 °C and 900 °C-1 in Figure 1.8(a)) coincide with each other at all target temperatures except 400 °C, as indicated in Figure 1.8(a). The significant difference at 400 ℃ is attributed to the softening and melting of the polymer coatings, aramid yarn, and sheath. In the following calculation of the Brillouin frequency shift, the second measurement on the mid-length Brillouin frequency was used as it represented the general trend observed inside the furnace under other applied temperatures. The W-DFOS experienced the same phenomenon at 400 ℃, but the B-DFOS did not. As shown in Figure 1.8(b), the Brillouin frequency shifted from 10.88 to 11.67 GHz when the target temperature increased from 20 C° (room temperature) to 900 ℃. The relationship between the temperature and the Brillouin frequency shift can be fitted satisfactorily by a linear or a parabolic equation. The parabolic equation showed a higher coefficient of determination (R^2=0.996) than the linear equation and can be used for data interpretation later. Similarly, the relationships between the temperature and

the Brillouin frequency shift for the W-DFOS and B-DFOS coatings were obtained and are presented in Figure 1.9.

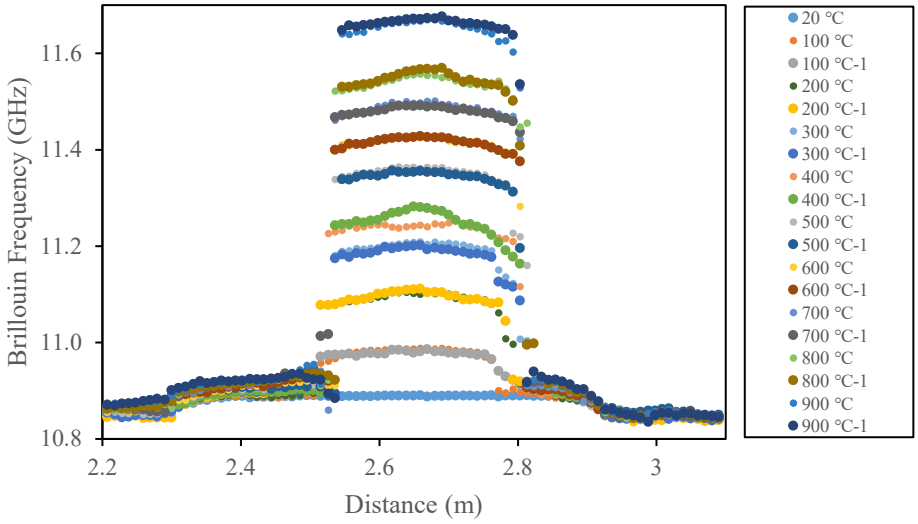

(a) Measured Brillouin frequencies along the length of optical fiber

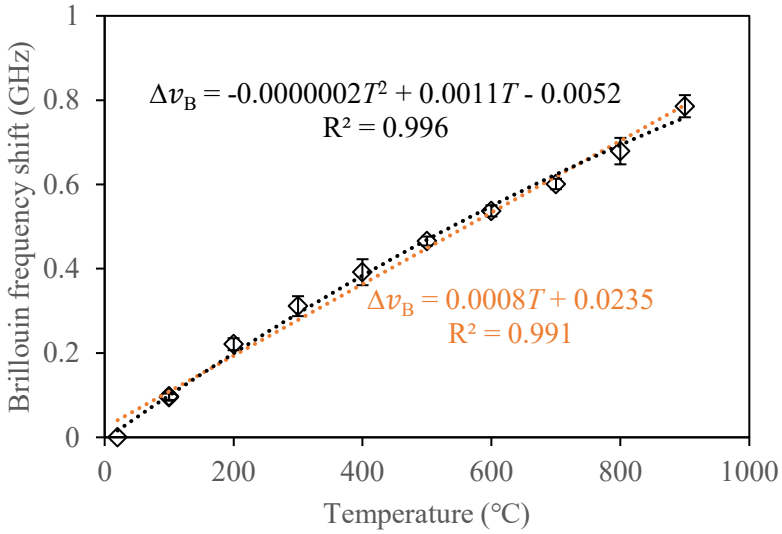

(b) Brillouin frequency shift at mid-length of the optical fiber versus temperature

Figure 1.8 Temperature calibration of one type of temperature sensor: Y-DFOS

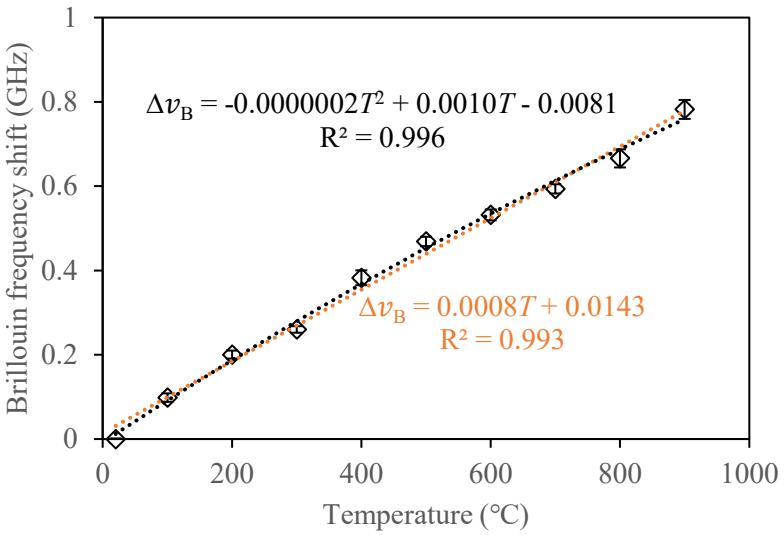

(a) W-DFOS

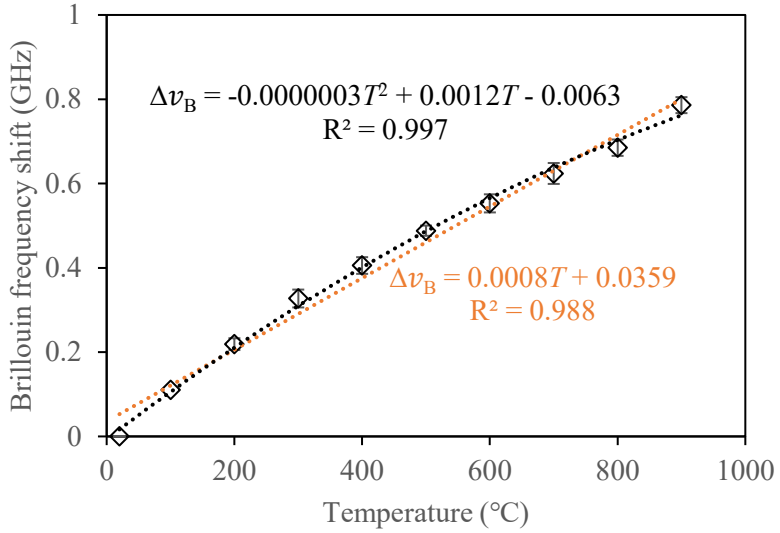

(b) B-DFOS

Figure 1.9 Temperature calibration of two types of strain sensors

Figure 1.10 shows the strain calibration results of the W-DFOS. Figure 1.10(a) shows a representative Brillouin frequency distribution along the length of the W-DFOS when subjected to a combined effect of varying elongations and constant temperature (400 °C). Each distribution

mainly consists of three segments: one inside the furnace region and two in the air. At the bottom of the furnace (around the 2.6 m mark), the gravity effect pulled cool air upward and mixed the cool air with the hot air inside the furnace, resulting in a temperature transition zone as observed in Figure 1.10(a). Figure 1.10(b) shows the Brillouin frequency as a linear function of the average tensile strain in the furnace region at each target temperature. The slope C_ε of each linear line in Figure 1.10(b) represents the strain coefficient (MHz/με) of the W-DFOS at a particular temperature. The strain coefficient is related to various target temperatures in Figure 1.10(c), which can be fitted by a linear equation with a coefficient of determination of 0.897. For any temperature distribution in application, the strain coefficient can be determined from the regression equation in Figure 1.10(c) and the strain distribution can be calculated by dividing the measured Brillouin frequency shift by the temperature-dependent strain coefficient. Similarly, Figure 1.11 presents the B-DFOS strain coefficient as a function of temperature, which is fitted by a linear equation with a coefficient of determination of 0.784. Note that the strain coefficients at 700 ℃ and 800 ℃ are not included in regression analysis because of their large deviations. In other words, the regression equation in Figure 1.11 is applicable to 600 °C only. In addition, the B-DFOS has a different fitting equation from the W-DFOS since the W-DFOS has an additional tight buffer, which may affect its cross section and stiffness during the softening and melting processes.

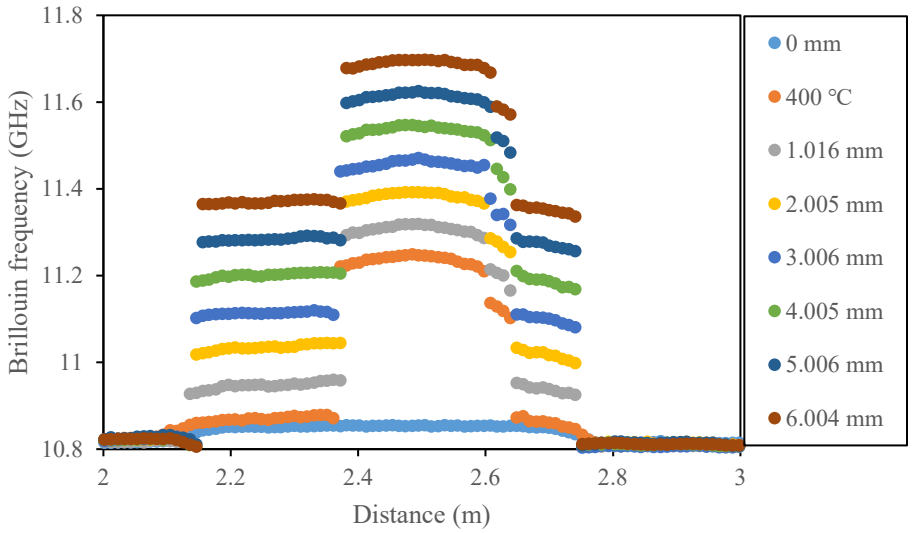

(a) Representative Brillouin frequency distribution at 400 °C

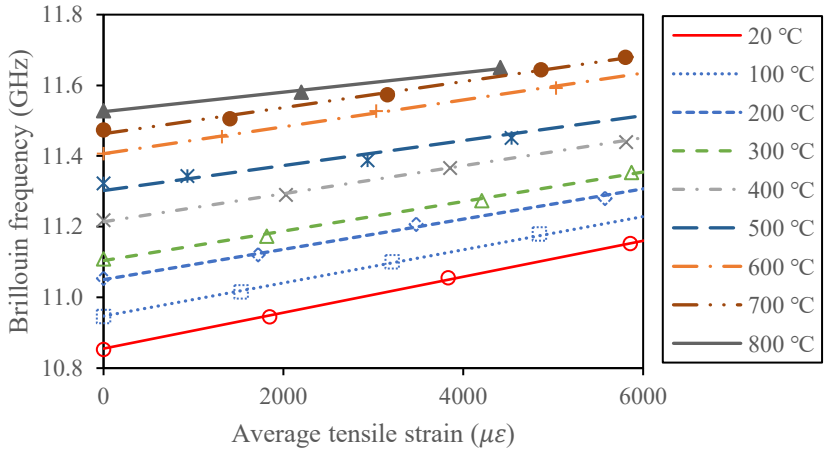

(b) Brillouin frequency versus average tensile strain at different temperatures

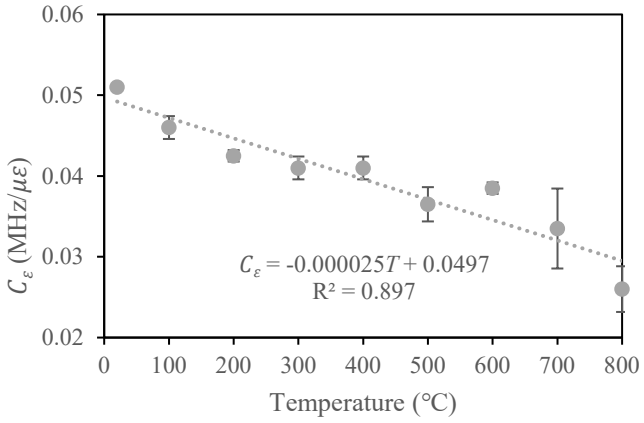

(c) strain sensitivity coefficient versus temperature

Figure 1.10 Strain calibration of the W-DFOS strain sensor

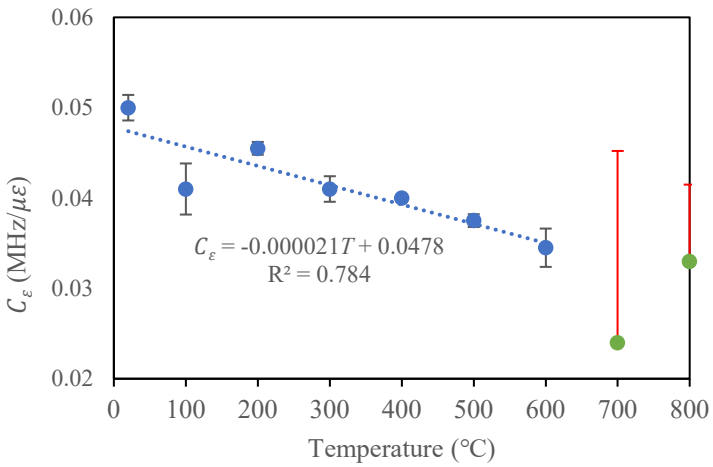

Figure 1.11 B-DFOS strain coefficient versus temperature relationship

1.4.3 Temperature Distribution along the Length of Mortar Specimen

Figure 1.12 shows the temperature distributions along the length of a mortar specimen, which were obtained from two Y-DFOS: one embedded inside the mortar (E-Y-DFOS) and the other attached on the surface of the mortar (S-Y-DFOS). Multiple measurements at different times were taken from the same specimen under a sustained target temperature to understand how long it took for the heating process to reach its steady state. Each measurement time at a specific target temperature represents the duration of the test at the sustained target temperature. For example, 100 ℃-7 min in Figure 1.12(a) means that the Brillouin frequency measurement has been taken from the E-Y-DFOS sensor 7 min after the furnace temperature reached 100 ℃. The measured Brillouin frequency was converted to the temperature measurement through the temperature calibration equation, as shown in Figure 1.8(b).

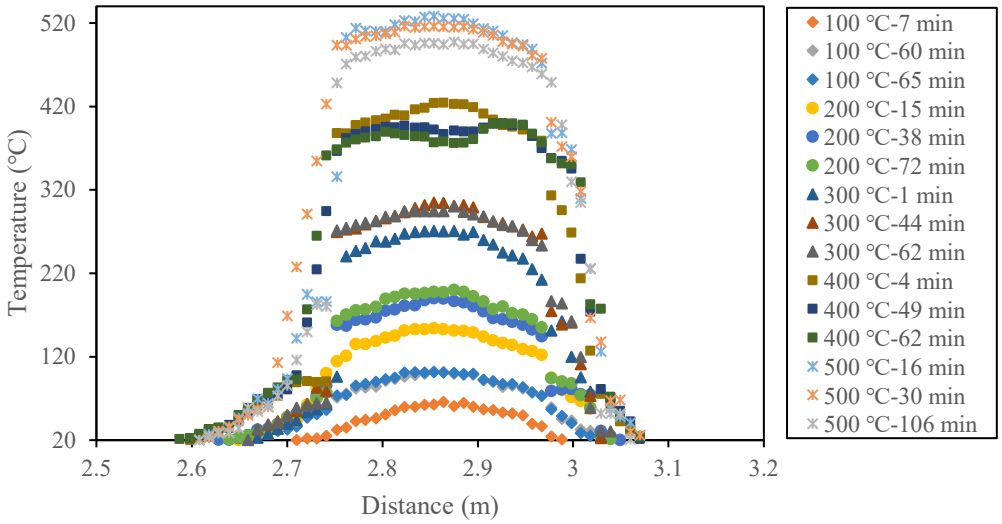

(a) The Y-DFOS embedded inside the mortar (or E-Y-DFOS)

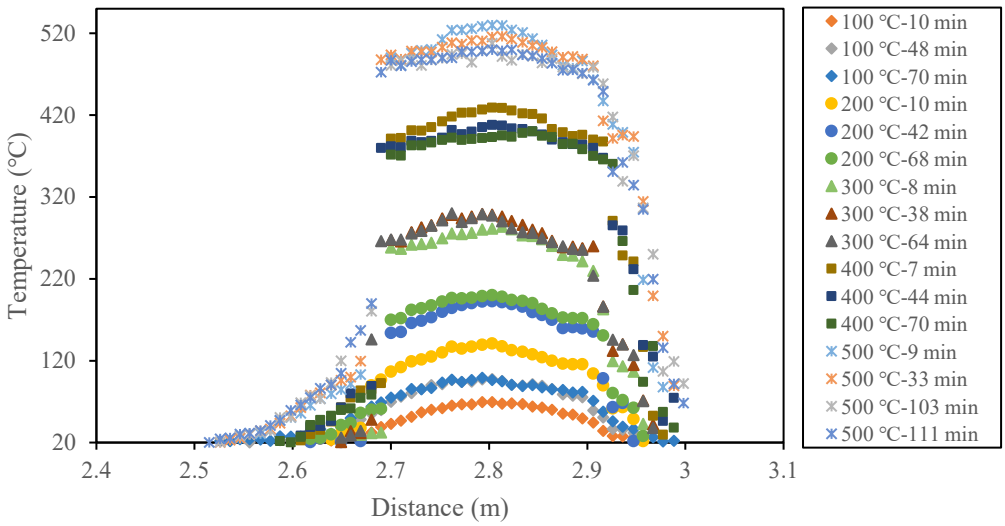

(b) The Y-DFOS attached on the surface of the mortar (or S-Y-DFOS)

Figure 1.12 Temperature distribution measured along the length of a mortar specimen

As shown in Figure 1.12, the temperature gradient from mid-length to the two ends of the sensor at 200 °C or higher was more significant than that at 100 °C due to increasing potential to bind the softening coatings or melting residuals with their surrounding mortar as the furnace

temperature increased. Equally important, the furnace temperature tapered off towards the two ends of the furnace where the hot and cold air circulation was significant at potential openings. Due to gravity, the measured temperature in the left transition zone corresponding to the top of the furnace was slightly higher than that in the right transition zone corresponding to the bottom of the furnace. The thermal expansion or shrinkage of these polymer materials introduced additional strain on the optical fiber and therefore modified the thermal response.

Figure 1.13 summarizes the maximum temperatures achieved at the mid-length of the mortar specimen, which were extracted from the temperature distributions recorded at different times in Figure 1.12 and compared the maximum measured temperatures with the target furnace temperatures. Some of the maximum temperatures (e.g., 400 °C and 500 °C) exceeded their corresponding target temperatures in a short time (e.g., 528.49 ℃ for E-Y-DFOS at 500 ℃-16 min). They approached the target temperatures after a long time (e.g., 497.33 °C for E-Y-DFOS at 500 °C-106 min.). The 'long time' in this series of tests was defined to be approximately 40 min, as indicated in Figure 1.13 for a stabilized heat transfer process inside the furnace. These observations indicated that the Brillouin frequency shift in the Y-DFOS sensor was caused not only by the increase of temperature but also by the strain induced at high temperature (500 °C). Although there was no bond or direct contact between the optical fiber and its protective sheath at the room temperature, the protective sheath, aramid yarn, tight buffer, and polymer coatings would soften and melt at 263-440 ℃, as indicated in Table 1.2. The excessively deformed softened coatings and their melting residuals probably stuck to the surrounding concrete, thus transferring the free deformation of mortar to the optical fiber. Furthermore, the induced strain was reduced over time because the difference in temperature between the mortar and the optical fiber decreased over time during the lateral heat transfer process surrounding the optical fiber.

The induced strain was compounded by the fact that the thermal expansion coefficient of polymer materials was 10^2-10^3 times higher than that of the glass fibers (Lu et al. 2018, Gu et al. 2013). Even over a relatively short length, the Y-DFOS was not strain-free at elevated temperatures of 300 ℃ or higher.

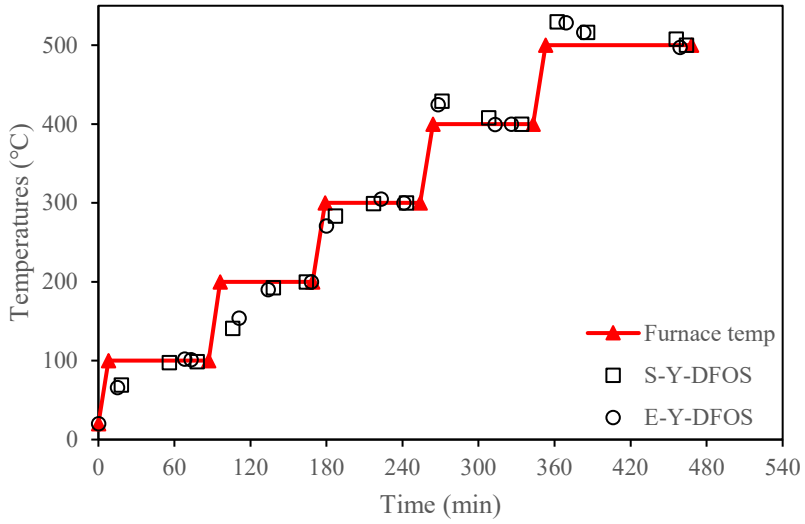

Figure 1.13 Change in maximum temperatures over time

1.4.4 Strain Distribution along the Length of Mortar Specimen

Figure 1.14 shows the strain distribution in the mortar specimen measured at different furnace temperatures from E-W-DFOS after the heat transfer process has been stabilized in about 40 min. To discriminate the strain and its associated temperature from the E-W-DFOS measurement, temperature compensation was conducted using Equation (1.1) with the aid of E-Y-DFOS for temperature measurement alone in theory. As needed, the temperature distribution from the E-Y-DFOS was interpolated or extrapolated to ensure its synchronization in time with that from the E-W-DFOS. After the temperature compensation, the Brillouin frequency shift was

divided by the strain sensitivity coefficient to determine the strain applied on every sampling point of the E-W-DFOS.

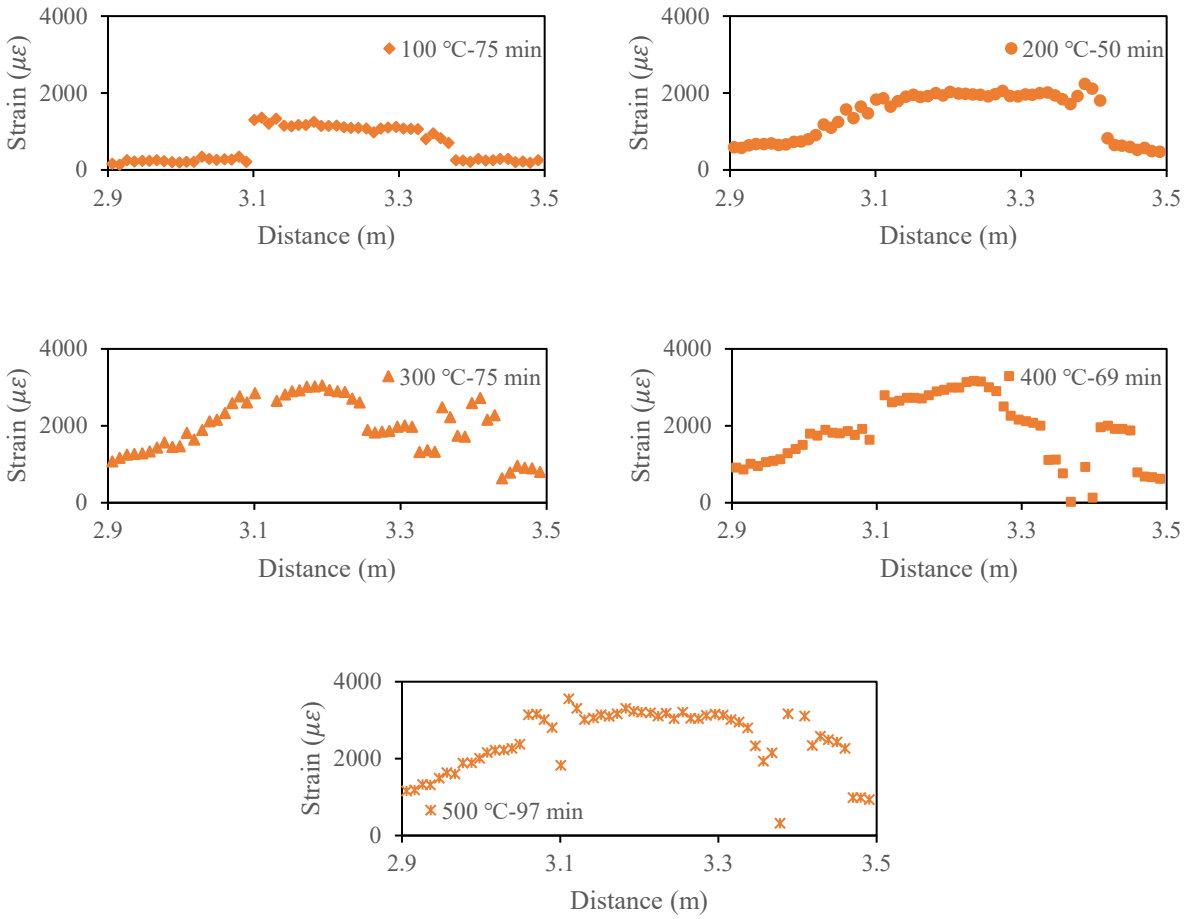

Figure 1.14 Longitudinal distribution of axial strains measured by E-W-DFOS

As shown in Figure 1.14, the strain distribution at each furnace temperature is non-uniform. The strain distribution is related to the temperature distribution, cement paste contraction or expansion, and sand expansion. Because of the heterogeneity of mortar, the uneven temperature distribution due to heat transfer through the mortar, and the uneven deformation transfer between the optical fiber and mortar matrix, the strain in the middle portion

is larger than the strain in the transition zone. Moreover, the strain distribution in the furnace region fluctuates/drops significantly at 300 ℃ −75 min. and 400 ℃ −69 min. due to polymer softening and melting effects and their induced unquantifiable bond condition between the optical fiber and the mortar. Once the coating was completely melted, the strain distribution inside the furnace at 500 °C became similar in shape to that at low temperatures.

Figures 1.15-17 show the strain distributions measured from S-W-DFOS, E-B-DFOS, and S-B-DFOS after at least 40 min of tests at sustained target temperatures, except for 4 min at 500 °C from the S-B-DFOS. At 500 °C, the S-B-DFOS broke after 4 min. Since the material properties of the protective layers and the adhesive layer govern the strain transfer between the optical fiber and mortar matrix at high temperatures, the type of DFOS (W-DFOS and B-DFOS) and their locations (surface bonded and embedded) affect strain measurements. In comparison with the S-B-DFOS in Figure 1.17, the S-W-DFOS in Figure 1.15 generally gives higher strains and more regular tri-linear strain distributions due to higher softening and melting temperatures as given in Table 1.2 and the presence of tight buffer whose softening and melting temperatures are even lower than those of the S-B-DFOS, also shown in Table 1.2. As the temperature increased, the tight buffer softened and melted before the coatings and gave more space for expansion of melted residuals, reducing the likelihood of binding to the nearby mortar and thus mixed strain effect on the Y-DFOS for temperature compensation. The above effect of a tight buffer on strain magnitude and distribution did not exist when the E-W-DFOS in Figure 1.14 was compared with the E-B-DFOS in Figure 1.16. Furthermore, the E-B-DFOS gave higher strains (especially above 300 ℃) than the S-B-DFOS due to its confined effect and effective strain transfer. On the other hand, the strains from E-W-DFOS and S-W-DFOS are nearly the same below 300 ℃.

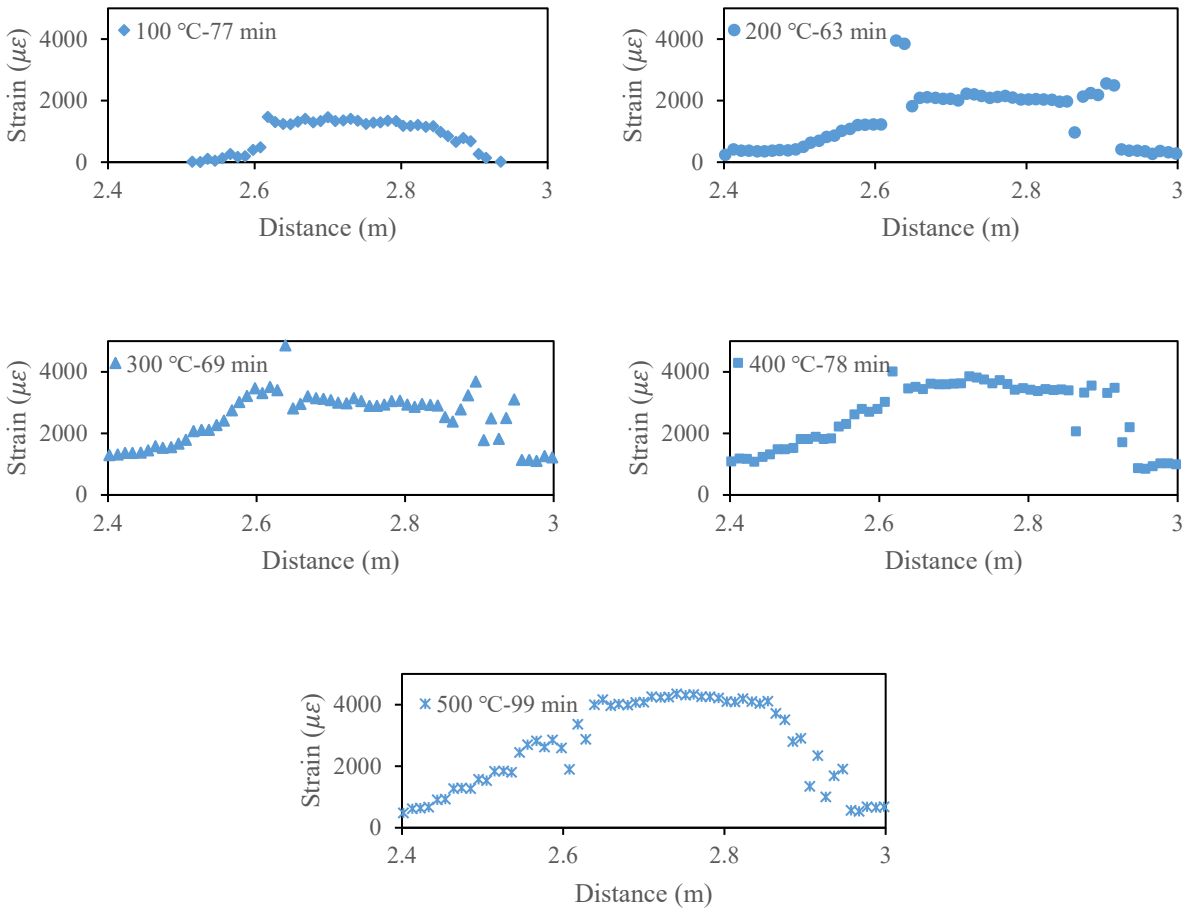

Figure 1.15 Longitudinal distribution of strains measured from S-W-DFOS

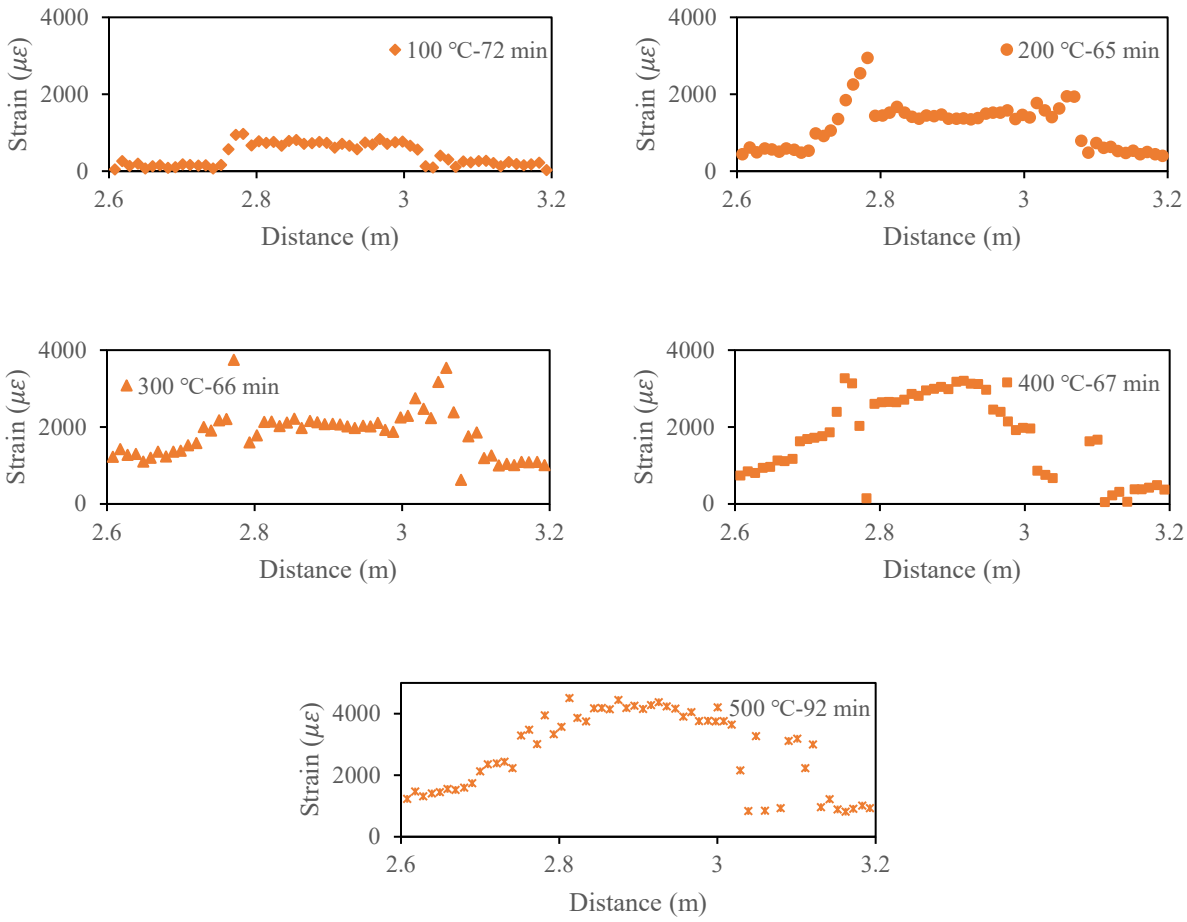

Figure 1.16 Longitudinal distribution of strains measured from E-B-DFOS

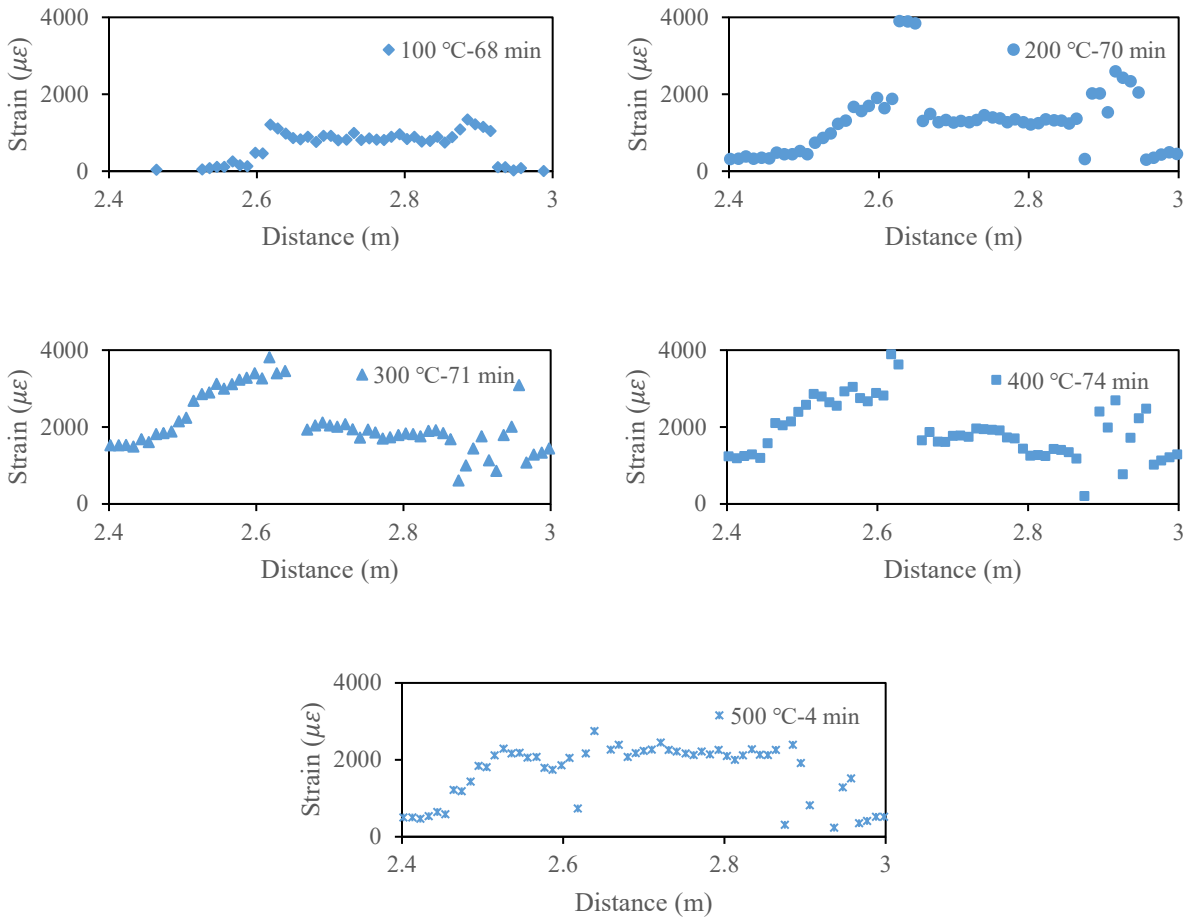

Figure 1.17 Longitudinal distribution of strains measured from S-B-DFOS

Figure 1.18 compares the strains at the mid-length of the mortar specimen between the DFOS measurement and thermal analysis. The 'thermal-induced strain' in Figure 1.18 was determined by multiplying the coefficient of thermal expansion of the mortar by the mid-length temperature in reference to the room temperature. The coefficient of thermal expansion of the mortar was determined by dividing the thermal expansion of mortar measured from a Linear Variable Differential Transformer (LVDT) by the measurement length and the temperature increment from the room temperature. Like the Ottawa sand, Illinois, U.S., the Missouri river sand used in this study has more than 80% of silica. Therefore, a thermal expansion coefficient

of 9.9×10^{-6} ℃$^{-1}$ (Cruz 1980) was used in this study. As seen in Figure 1.18(a), the W-DFOS measurement gave higher strains than the thermal-induced strains at 100 ℃ to 300 ℃ due to the dominant thermal effect when the thermal expansion coefficient of the tight buffer was 10^2-10^3 times higher than that of glass, but lower strains at 400 ℃ due to the dominant mechanical effect with the reduction in strain transfer efficiency caused by softening and melting of the polymer. On the other hand, the measured strain from the B-DFOS was in good agreement with the thermal-induced strain at 100 ℃ but smaller than the thermal-induced strains at 200 ℃, 300 ℃, 400 ℃, and 500 ℃. In general, the maximum error between the measured and calculated strains is up to 23% at 200 ℃. At 300 ℃ or higher, the measured mid-length strains significantly deviate from the calculated thermal-induced strain.

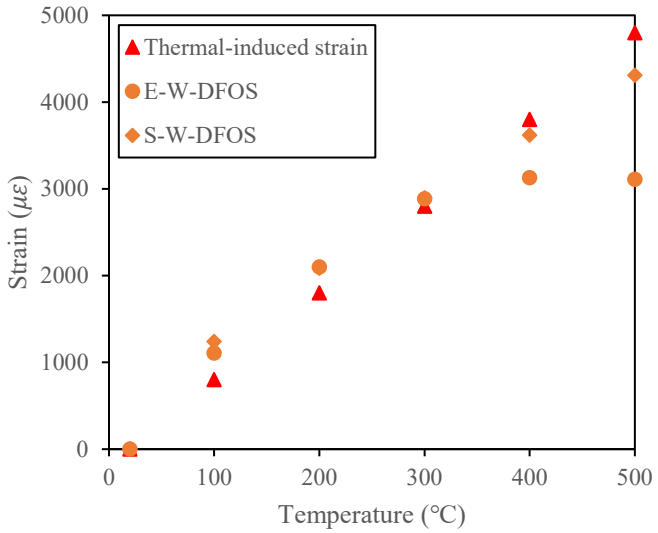

(a) W-DFOS

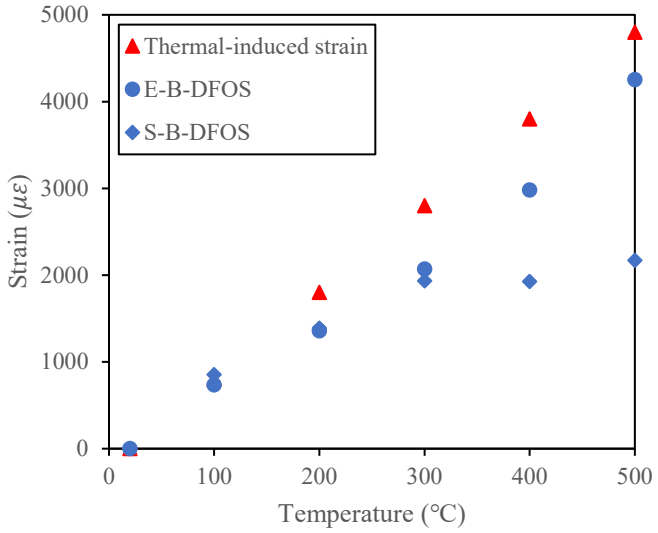

(b) B-DFOS

Figure 1.18 The DFOS measured strain versus the calculated thermal-induced strain at the mid-length of the mortar specimen

1.4.5 Free-expanded Thermal Displacement of the Cantilevered Mortar Specimen

The strain distribution curves presented in Section 4.4 can be integrated to determine the free-end thermal displacement of the cantilevered mortar specimen. The thermal displacements

based on the strain measurements from two DFOS are summarized in Figure 1.19 as a function of a target temperature. Each point represents the average value of the integrated results from the strains measured at different time durations corresponding to each target temperature. At high temperatures, the thermal displacement is contributed by the expansion or contraction of cement paste (i.e., hydration products), the expansion of sand, dehydration of solid matrix, and the loss of moisture (free water in pores and voids and water chemically bounded to hydration products). Figures 1.19(a) and 19(b) include regression fitting curves for the W-DFOS and B-DFOS measured displacements, respectively. For each sensor, the obtained displacement data can be well fitted by a parabolic equation particularly below 200 °C. The slope of the parabolic curve gradually decreases from the ambient temperature to 500 ℃. The coefficients of determination are 0.932 and 0.877 for the W-DFOS and B-DFOS, respectively. The displacement data above 300 ℃ show significant scattering due to the softening and melting of polymer coatings and buffer.

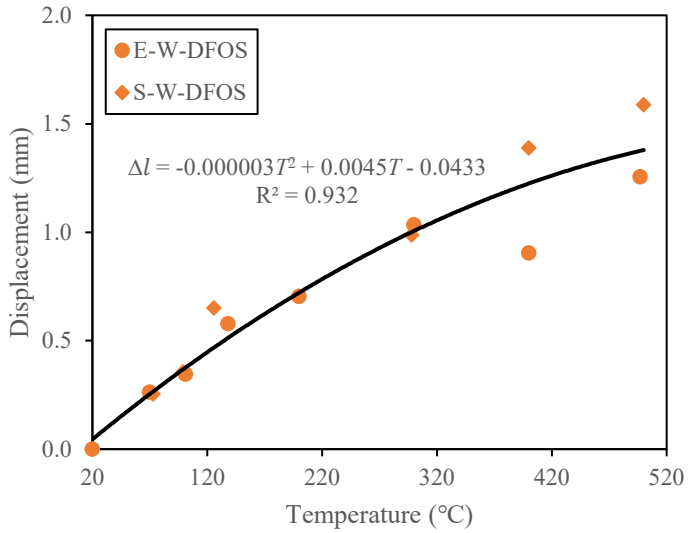

(a) W-DFOS

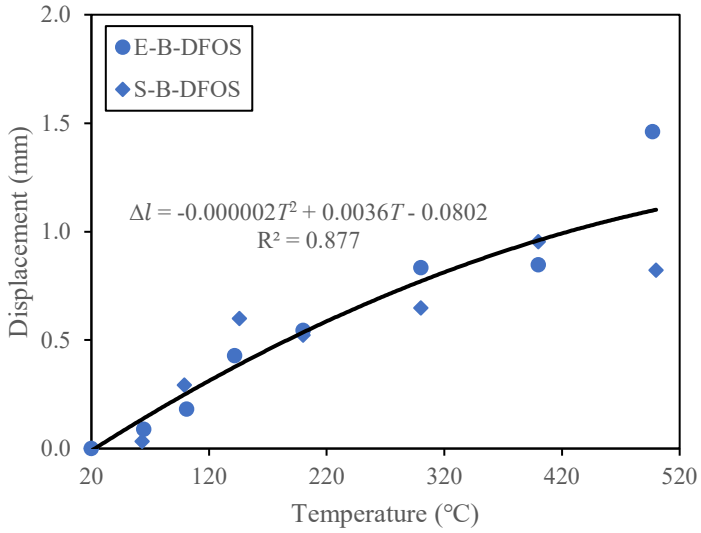

(b) B-DFOS

Figure 1.19 Thermal-induced deformation measured from various DFOS installations

1.5 Summary

Due to their compactness and electromagnetic immunity, polymer-packaged optical fibers widely used in the telecommunication industry are a promising, cost-effective, rugged,

distributed sensing technology for the in-situ measurement of strain and temperature in performance-based fire engineering of buildings. While critical in protecting optical fibers from damage during deployment, the soft polymer coating introduces uncertainties on the way that the optical fibers respond to their surrounding temperature and strain effects. Based on the extensive sensor tests and PPP-BOTDA of three commercial products (B-DFOS, W-DFOS, and Y-DFOS) deployed in mortar specimens as well as the thermogravimetric analysis of their protective polymer layers, the following conclusions can be drawn:

- For sensor calibrations, the temperature and strain coefficient equations are applicable up to 900 °C and 600 °C, respectively. For material characterizations, the melting temperature of the B-DFOS coatings, buffers, and sheaths ranges from 281 °C to 315 °C while the W-DFOS coatings and aramids melt in a temperature range of 344 °C to 440 °C.
- When embedded inside a mortar specimen or bonded on the mortar surface, the Y-DFOS is no longer strain-free over 300 °C, even with its sheath and tight buffer separated by aramid yarns. This is because the softening and melting polymer layers can be fused together and stick to surrounding mortar at that level of temperature. Due to the varying material properties of additional polymer layers in heat transfer, both the Y-DFOS and W-DFOS show time-dependent Brillouin frequency shifts that take over 40 min to achieve heat balance at a target temperature while each PPP-BOTDA measurement takes approximately 0.5 min. Due considerations must be taken to understand fire dynamics and estimate temperature ranges so that the DFOS can be properly applied in engineering practice.

- Under high temperatures at its middle portion, a cantilevered mortar specimen is subjected to unevenly distributed strains due to mortar heterogeneity, non-uniform temperature distribution, and temperature-dependent strain transfer efficiency. From 100 ℃ to 300 ℃, the W-DFOS measured strains at the middle portion are larger than the free-expanded thermal strains likely because of a high thermal expansion coefficient of the additional tight buffer. At 400 ℃ and 500 ℃, however, the strains at the middle portion are smaller than the thermal-induced strains. The displacement data obtained by integrating the distributed strain measured follow a consistent trend till 300 ℃ and then begin to scatter. Overall, the displacement is well correlated with temperature up to 500 °C with a coefficient of determination of 0.877 or higher.

Although the DFOS technology in this study provides a new path for strain and temperature measurements, the application of the three fibers is relatively new at the present time. The significant contribution to civil engineering can be manifested as time goes by. It is envisioned that the distributed strain and temperatures measured in engineering structures under fire conditions can be uniquely used to develop and validate fire dynamic simulations, heat transfer models, and finite element model updating. In addition, the limitations of the three fibers for strain and temperature measurements have been identified mainly from polymer coating layers. Further improvements can thus be made to the fiber optic sensors in future studies. As an example, metal coatings may be used to protect the glass cladding and core of an optical fiber.

Chapter 2 Spiral Deployment of Optical Fiber Sensors for Distributed Strain Measurement in Seven-Wire Twisted Steel Cables, Post-Tensioned against Precast Concrete Bars

2.1 Introduction

Steel cables are typically used in bridges and prestressed concrete structures, and they have large cross-sectional areas that are subjected to large tensile forces (Yao et al. 2021). The rupture of the cable may lead to the progressive collapse of the structures and catastrophic outcomes (Zhang et al. 2021). For prestressed concrete structures, effective prestressing force, and short-term or long-term prestress losses affect the concrete cracking resistance, deflection, load-bearing capacity, and durability (Abdel-Jaber and Glisic 2019a). Therefore, the condition of the cables used in construction and operation directly determines their structural safety and performance. The cable force becomes critical to evaluating the cable and the structural health condition. Measuring the cable force is helpful in monitoring and assessing the health condition of cable-based structures. Different methods have been developed to measure cable forces, including the traditional direct strain measurement method, the oil pressure meter method, the low-cost vibration frequency method, the high-accuracy magnetic flux sensor method in the lab., and acoustic emission technology (Abdel-Jaber and Glisic 2019b). Although these methods have achieved great success in cable force measurement in engineering structures, some limitations can be found (Kim et al. 2012, Zhu et al. 2021, Huynh and Kim 2017). For example, magnetic flux sensors are easily interfered with by electromagnetic fields; indirect vibration-based measurements need to further improve their accuracy and robustness; and strain gauge sensors need temperature compensation, and their long-term stability is a concern, especially in harsh environments. Moreover, many strain sensors are needed to measure forces along the cables (i.e., for a long measurement distance) and the installation of these sensors increases the cost and complexity. In addition, numerous wires for connecting these sensors cannot be handled easily,

which affects construction and operation, and even destroys structural performance. Therefore, more effective cable force measurement methods still need to be developed to achieve in situ and on-time monitoring.

In recent years, fiber optic sensors have been used to measure cable forces. The use of fiber optic sensors has many advantages (Zhang et al. 2021, Zhang et al. 2020). Their very light weight and small dimensions reduce the potential installation effect of fiber optic sensors on the mechanical performance of the cables. Their electromagnetic interference immunity improves measurement robustness and reliability. Moreover, based on Rayleigh and Brillouin scatterings (Güemes et al. 2010, Murayama et al. 2011, Rizzolo et al. 2015, Liang et al. 2021), fully distributed strain measurements along the optical fiber have been developed. Fully distributed measurements have the advantages of identifying local interactions that are induced by friction contact between the cable and the duct, and local slip along the cable embedded in the concrete from uneven strain distributions. In the literature, Brillouin-scattering-based distributed sensing technologies have been applied to measure cable forces. Zhou et al. (2009) and He et al. (2013) developed a smart fiber-reinforced polymer rebar with an embedded optical fiber, and this smart rebar and six wires were bundled as a whole to be used for post-tensioned concrete structures. It has been demonstrated that this smart rebar could monitor prestress loss through the testing of a post-tensioned concrete beam and a prestressed steel frame structure. Although the Brillouin optical time domain analysis (with low spatial resolution) has been applied to achieve a distributed prestress condition assessment, the availability and packaging complexity are limiting smart rebar applications. In addition, the deformation compatibility between the smart rebar and the surrounding wires is required. Once damage occurs at the local area of the smart rebar, the optical fiber may fail to measure prestress loss. The same research group (Lan et al. 2012, Lan

2011) used the smart steel strand with a smart rebar, which was instrumented with the optical fiber, to monitor the prestress loss of damaged reinforced concrete structures. The reinforced concrete structures were loaded to the initial cracking stage and the normal service limit state, then they were unloaded to zero. The instant prestress loss during the tensioning process was not identified, and the prestress loss during the unloading process was not emphasized, which means that the prestress reduction due to the removal of the external load was not determined, and the actual prestress loss was, seemingly, unknown. Butler et al. (2016) and Ye et al. (2020) used distributed fiber optic sensors (DFOSs) to evaluate the early-age behavior of full-scale prestressed concrete beams. Brillouin optical time domain reflectometry strain sensor cables were installed to the underside of the prestressing strands using plastic cable ties. Although the integrated fiber optic sensing system can be a promising tool for short- or long-term concrete bridge strain monitoring, more details about the installation of these sensor cables to the strands were not given. Webb et al. (2017) applied the Brillouin optical time domain reflectometry technique to monitor the strain of a three-span, pretensioned, prestressed, concrete beam-and-slab bridge in the field. The fiber optic cables were embedded in the concrete. The prestressing strands only provided supporting positions because the fiber optic cables were attached to the strands near the ends or to several local points by the tape. Attention was paid to reduce the potential optical fiber cables' effect on the bond between the sensor cables and the prestressing strands. Moreover, Ansari's research group (Nazarian et al. 2016, Scarella et al. 2017) used the Brillouin optical time domain analysis technique to monitor cables' tension loss under static and dynamic loading. Both tests were conducted on a scaled cable-stayed bridge, in the lab, and DFOSs were instrumented on the bridge deck. Recently, Li's research group (Xu et al. 2016) used the differential pulse-width pair with Brillouin optical time domain analysis to measure

strain distributions along the whole length of a 1108 m suspension bridge, and the bridge design was evaluated by the measurement data. Overall, the use of DFOSs, based on the pulse-pre-pump Brillouin optical time domain analysis, to directly measure cable forces is still lacking and is not comprehensive.

As an emerging new cable force measurement technology, the distributed sensor design and installation needs to be clarified and validated. To advance the innovative application of DFOS, based on Brillouin scattering, this study proposes a spiral optical fiber deployment scheme to measure cable forces in concrete during tensioning processes (i.e., before and after prestressing force release). The experimental test setup, the DFOS instrumentation scheme, as well as the tensioning system and the procedures are described in the next section of this paper. The proposed cable force measurement effectiveness was demonstrated by comparing the collected DFOS data with the load cell values. The relationships between the optical fiber-measured results and the ground truth cable force were established, and the instant prestress loss for the present test setup was identified from the distributed fiber optic sensing data. This study provides a new deployment scheme to measure cable forces by using distributed fiber optic sensing technology.

2.2 Experimental Program

2.2.1 Material properties

The concrete used in this study was designed in accordance with the mix proportions as shown in Table 2.1. The concrete included cement, fly ash, river sand, coarse aggregate, air-entrained agent (DAREX® AEA), high range water reducer (HRWR-ADVA 198), and viscosity-modifying admixture (CONCERA CP 1124). Among them, the coarse aggregate with a size range between 9.5 and 12.7 mm was from the Capital Quarry, Sullivan, Missouri, and the

riverbed siliceous sand was from the Capital Quarry, Jefferson City, Missouri. The macro fiber (brand name: STRUX BT50) was mixed in the concrete. It had a fiber length of 50 mm and aspect ratio of 75 as shown in Figure 2.1(a). Its tensile strength and elastic modulus were 550 MPa and 7 GPa from the supplier. The specific mix procedures for concrete are as follows. The coarse aggregate and fiber were added to the sand and mixed for two minutes. Then, half of the water mixed with AEA was added to the mixer and mixed for over a minute. After that, the cement and fly ash were added, and the mixing continued for another minute . Then, ¼ of the water mixed with ¾ of the HRWR was added to the mixer and mixed for over another minute, and the remaining ¼ of the water mixed with the VMA was added for another three minutes of mixing. The final ¼ of the HRWR was used to adjust the mixture fluidity (i.e., slump flow over 500 mm). Before the concrete was ready for casting, the concrete was mixed for another two minutes. Note that the fiber was gradually added during the whole mixing procedure to guarantee a relatively uniform distribution.

(a) (b) (c)

Figure 2.1 (a) Fiber appearance and fiber length of 50 mm; (b) Concrete mixture in a mixer with a capacity of 170 L; (c) Compressive test for cylinder concrete specimen.

Figure 2.1(b) shows the concrete mixture ready for use. The concrete compressive test was performed as shown in Figure 2.1(c). The cylinder specimen dimensions were 100 mm diameter by 200 mm length. The tested average compressive strength was 52.5 MPa. The nominal diameter of the 7-wire steel prestressing strand was 12.7 mm, and the nominal cross area was 98.7 mm^2. The mass/meter ratio was 0.88 kg/m. The ultimate tensile strength was 1860 MPa and the elastic modulus was 200 GPa. Also, the center wire diameter was 4.3 mm, and the outer wire diameter was 4.2 mm.

Table 2.1 Mix proportions of concrete

Components	Content
Cement (kg/m^3)	260
Fly ash (kg/m^3)	110
River sand (kg/m^3)	1020
Coarse aggregate (3/8-4/8 in) (kg/m^3)	750
AEA (L/m^3)	0.3
HRWR (L/m^3)	2.6
VMA (L/m^3)	3.3
BT50 fiber (kg/m^3)	3.0

Table 2.2 Fiber properties

Items	STRUX BT50
Material	Polypropylene
Shape	Straight
Color	White
Cross-section	Rectangle
Specific gravity	0.91
Length (mm)	50
Width (mm)	0.667
Aspect ratio	75
Thickness (mm)	0.25
Elastic modulus (GPa)	7
Tensile strength (MPa)	550
Absorption	None
Melting point	160 ℃
Ignition point	570 ℃
Alkali, acid, and salt resistance	High
Addition rate (kg/m^3)	4.0-9.0

2.2.2 Specimen design and preparation

Eight post-tensioned prestressed concrete specimens were designed, and all concrete specimens had the same dimensions. The specimen dimensions were 1.219 m long, and 100 mm by 100 mm cross-section. A 25.4-mm-diameter duct was reserved at the center of the cross-section of the specimens as shown in Figure 2.2. Moreover, two tee sockets (i.e., pipe fittings) were used in each specimen for connecting the pipe segments as a whole and the vertical opening could be used for grouting later. The test parameters (see Table 2.3) included bonded/unbonded prestressing strands, presence of paper tape defects and duct materials (plastic and metallic) as well as different adhesives for bonding DFOS to the strand. In this study, the aim is to measure the cable force using DFOS during the tensioning process. Therefore, the effect of these parameters on the prestressing force change can be neglected. However, the effect of these parameters on the force after grouting and under high temperatures will be reported later. In the process of concrete casting, a rebar was inserted into the duct to provide sufficient supporting

force and keep the duct straight. Figure 2.2(c) shows concrete casting into the molds. During demolding, the supporting rebar was taken out. After that, they were moved to a standard curing room before post-tensioning steel strands. The steel strands with desirable length were cut for DFOS instrumentation and the surface of the concrete specimens was grinded and cleaned before posttensioning steel strands.

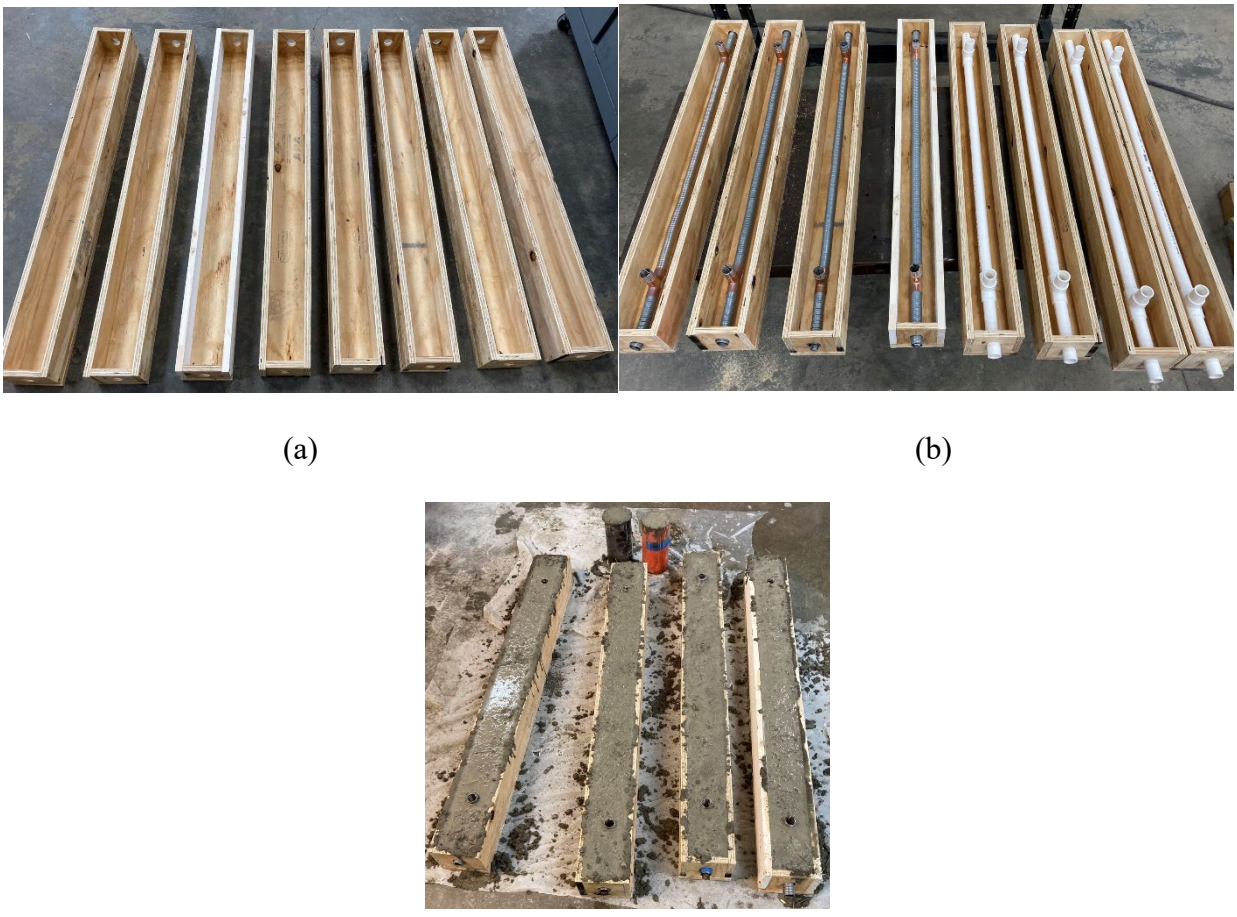

(a) (b)

(c)

Figure 2.2 Specimen fabrication: (a) mold assembly; (b) plastic pipe and corrugated steel duct for post-tensioning strand and grouting; (c) casting specimens.

Table 2.3 Specimen design with different parameters

Specimens	Bonded/unbonded	Adhesives	Paper tapes for defects	Duct materials
PC1	Bonded	Normal epoxy	No	Plastic
PC2	Unbonded	Normal epoxy	No	Metallic
PC3-1	Bonded	Normal epoxy	Yes	Plastic
PC3-2	Bonded	Normal epoxy	Yes	Plastic
PC4-1	Bonded	Normal epoxy	Yes	Metallic
PC4-2	Bonded	Normal epoxy	Yes	Metallic
PC5	Bonded	High temperature	No	Plastic
PC6	Bonded	Normal epoxy	No	Metallic

2.2.3 Distributed fiber optic sensing principle

Pulse-pre-pump Brillouin optical time domain analysis (PPP-BOTDA), stimulating the phonon with a long-duration pulse before a short-duration pulse arrives, measures temperature and strain changes by relating them to the change in the refractive index of an optical fiber and the speed of acoustic wave traveling along the optical fiber. As shown in Figure 2.3, a probe continuous wave and a pump pulse wave counter-propagating were sent from two ends of an optical fiber. Once the frequency difference between the continuous and pulse waves matches the optical fiber Brillouin frequency, Brillouin loss or gain occurs, associated with the fiber medium density. The density and refractive index are affected by both strain (ε) and temperature (T), while the Young's modulus and Poisson's ratio are affected by temperature (T) only (Bao and Chen 2016a, Bao and Chen 2015). Therefore, strain and temperature changes in the optical fiber cause a shift in the Brillouin frequency. For a change in strain and temperature from reference values obtained during calibration, the Brillouin frequency shift (Δv_B) can be expressed as:

$$\Delta v_B = C_\varepsilon \Delta\varepsilon + C_T \Delta T \tag{2.1}$$

where C_ε and C_T represent the strain and temperature sensitivity coefficients, respectively. Spatially distributed Brillouin gain spectra are measured along the length of the tested single mode optical fiber using a Neubrescope data acquisition system (Model NBX 7020), from which the Brillouin frequency is determined using a Lorentz curve fitting algorithm. Because the tensioning process was conducted at the constant lab environment, the temperature change can be considered zero. Therefore, only the first term (i.e., strain change) induced a Brillouin frequency shift. In this study, an optical fiber with a buffer layer (in addition to the outer coating, inner coating, cladding layer, and glass core) was used for sensing strain. From the lab calibration test (i.e., uniaxial tensile test), the strain frequency shift coefficient for the optical fiber is 19570.1 $\mu\varepsilon$/GHz at ambient temperature. PPP-BOTDA has a high spatial resolution of 2 cm (at 0.2-ns pulse width) and kilo-meter order measurement distance, which is better than the spatial resolution of 15 cm or even larger in traditional BOTDA and Brillouin optical time domain reflectometry (BOTDR). Also, 15 $\mu\varepsilon$ and 0.75 ℃ measurement accuracies can be respectively achieved for strain and temperature with an average count of 215 in PPP-BOTDA.

The Neubrescope NBX-7020 (Neubrex Co., Ltd., Japan) data acquisition system can achieve both Brillouin and Rayleigh scatterings. The measurement accuracies of Brillouin scattering can potentially be improved by approximately seven times in temperature and 15 times in strain using Rayleigh scattering. However, the cross-correlating two-by-two measurement approach is needed to increase measurement accuracy by correlating the current measurement with the immediately past reference (i.e., zero point) for Rayleigh scattering. Due to the requirement for cross correlation between any two sequential measurements, the applied strain steps (several tens of microstrains) or temperature steps must be sufficiently small to ensure accurate measurement of a corresponding minimal frequency difference in Rayleigh scattering.

The overall strain or temperature effect can be accumulated by summing all steps. When the strain difference exceeds 500 $\mu\varepsilon$, the cross correlation in the tunable wavelength coherent optical time domain reflectometry (TW-COTDR) is prone to fail as verified experimentally in a previous study. Therefore, the Brillouin sensor is selected for prestressing force monitoring since prestressing force usually induces a large amount of strain in the steel wires during the tensioning process.

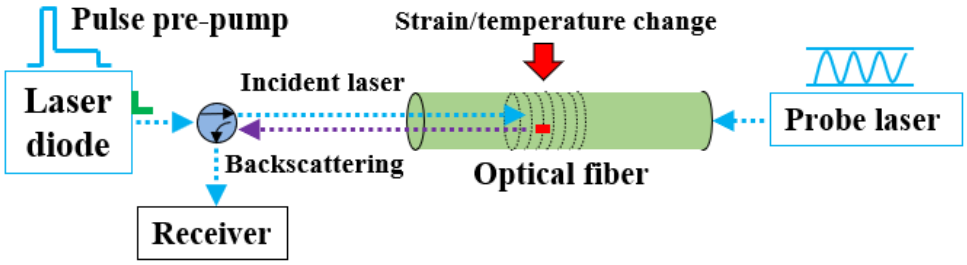

Figure 2.3 PPP-BOTDA working principle.

2.2.4 Instrumentation and loading

Two kinds of DFOS were instrumented on each steel strand. One measured the strain and temperature simultaneously, while the other measured only the temperature. Two optical sensors were prepared for each type to avoid unexpected damage, increase surviving rate, and data repeatability. These DFOS were kept helix along the valley between the adjacent outer surface wires and parallel along the outer wires. Using the spiral DFOS shape avoided easy debonding and fracture compared to a straight instrumentation scheme. A small tension was applied during installation, which would cause an initial strain condition. However, this initial condition would not affect the measured results because it was used as the reference for later measurement results. Figure 2.4(a) shows these DFOS arrangements along the strand. The paper tapes were used to fix

the temperature sensors along the strand. However, liquid glue was first applied to the strain sensors. Then, a two-part epoxy (i.e., Loctite brand, USA) was used to bond the strain sensors to the strand and at least 24 hours were needed for the epoxy hardening. Note that a hi-purity alumina adhesive (supposed to have high temperature resistance) from MTI Corporation, USA was used for the PC5 specimen to see an adhesive type of effect on the measured results. From Figure 2.4, the bond length to the steel strand can be seen, which is not equal to the center distance of the two small holes (see Figure 2.2). A small reduction from the center distance (about 1 cm from each end) can be observed, facilitating taking the DFOS out from the duct later and reducing DFOS damage risk during tensioning. Before the strand instrumented with DFOS was put inside the duct, the small concrete pieces inside the duct coming from demolding and surface cleaning were cleaned. The steel plates with a thickness of 12.7 mm were bonded to the specimen ends using a two-part epoxy (i.e., tank bond brand or Loctite brand, USA) to reduce the stress concentration at the anchor location after releasing the prestressing force. At the same time, the two ends of each fiber sensor were numbered for later splicing and easy distinguishment because two ends are needed for PPP-BOTDA measurement (i.e., probe and pump ends). Careful attention should be paid when placing the strand instrumented with DFOS inside the duct to avoid any damage and fracture, especially for the strain sensors with less protective layers. However, the friction between the strand and the duct surface cannot be avoided due to the weight and length of the strand during placement. After the strand was carefully placed inside the duct, the DFOS lead portion was taken out from the small, reserved holes using a fishing hook as shown in Figure 2.4(b) to avoid damage caused by anchoring the strand. It would be very tight and the DFOS damage may occur if the DFOS went along the strand.

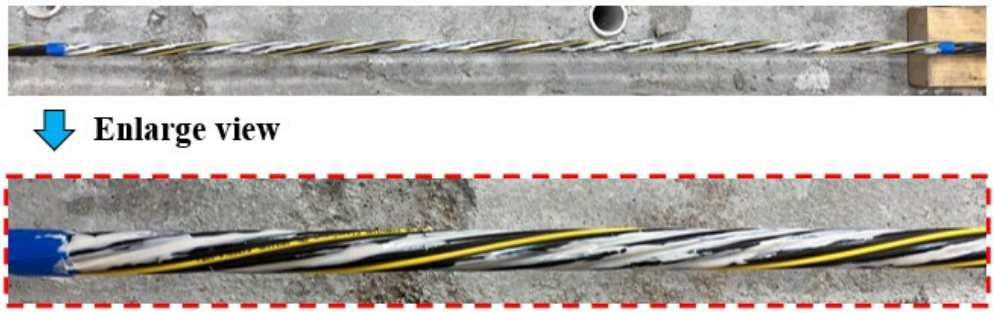

(a)

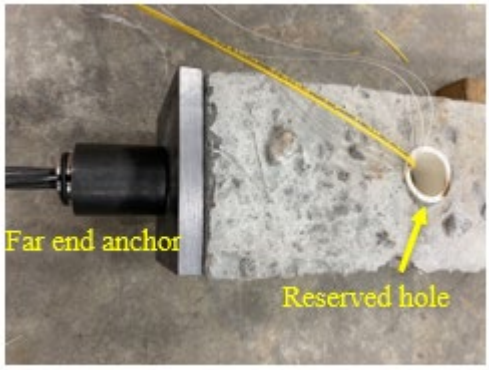

(b)

(c)

Figure 2.4 (a) Distributed fiber optic sensors instrumentation on the steel strand; (b) DFOS taken out from the reserved holes; (c) cross-section of a steel strand with optical fibers**.**

To observe the bond between the optical fiber and strand in a cross-section, a segment of the steel strand instrumented with two DFOSs covered by the epoxy was cut from a long specimen sample, which was first loaded to 57.8 kN (approximately equal to second load level) and unloaded. Figure 2.4(c) shows the cross-section cut from the sample. Several layers of paper tapes and two clips were used to fasten the strand at the cutting area and to avoid wire rotation since the cutting process may induce stress release in these twisted wires. Although this effort has been made, the mechanical damage can still be observed as highlighted red dashed lines in

Figure 2.4(c). Some findings from these image observations are as follows. The epoxy has a good bond to the steel strand in addition to the mechanical damage. Since the optical fiber was placed at the valley between the adjacent two wires first and the viscous epoxy covered the optical fiber, the optical fiber 1 was encased by the epoxy due to the fluidity, while an unfilled void can be observed at the bottom triangle region where the epoxy could not arrive near the optical fiber 2. Any movement of optical fiber during the covering process affected final optical fiber position and epoxy fullness on the cross-section. Therefore, the position uncertainty and the void defect (probably distributed along the strand) from the optical fiber installation are responsible for the measured errors of the prestressed forces from DFOS, as compared with the load cell values.

The test setup for applying prestressing force is shown in Figure 2.5. A costume-designed steel block for tensioning was used. A hydraulic jack with a maximum capacity of 30 tons and an effective contact area of 4658 mm^2 (7.22 in^2) for the cylinder was used. The specific tensioning procedure is as follows. First, the far end of the steel strand was anchored. After the load cell was installed at the tensioning end as shown in Figure 2.5(a), the prestressing force was manually applied by the cylinder. Once the targe prestressing force value reached, a hammer was used to solidate the anchor chucks at the tensioning end to make a tight anchor and reduce prestress loss once the force was released. However, the instant prestress loss due to the anchor retraction, steel plate and epoxy deformation, and elastic deformation of the concrete specimen cannot be avoided. After the force was released (less than 10 seconds) by the cylinder, the tensioning process was finished. Note that during the tensioning process, the concrete specimen was not subject to any applied force and the prestressing force was applied on the specimen after anchoring and then released. Three (or four) load steps were performed, namely 6.5%, 32.5%,

and 65%, (and 75%) of the ultimate strength of the steel strand. At the final load step, an extra 5% force was applied to improve the prestress level in the strand after instant prestress loss. At each load level, several-time DFOS measurements were conducted, and the oil pressure meter readings were recorded as well. For the load cell, its readings can be automatically recorded from the beginning. However, after the force release, the oil pressure meter and load cell did not work, and the prestress force on the cable can be monitored by the DFOS in this test setup, which highlights the advantage of the DFOS technology to measure on-time cable force distribution and long-term prestress loss due to concrete shrinkage and creep. Figure 2.5(b) shows the overall test setup for one testing specimen. Note that the oil pressure meter was only used for specimen PC1. A brief discussion for the DFOS survivability at the high load may be of interest to the readers. From Gao et al.'s study (2006), the optical fiber bonded to the steel strand can measure the stress of about 1100 MPa (out of 1860 MPa), although their nominal cross-sectional area of the strand was about 140 mm^2; it was suggested to use 60% of 1860 MPa as the tensioning force from their conclusion. However, in this study, the tensioning force is extended to 65% or 75% of the ultimate strength of the strand and it is found that the DFOS covered by the epoxy survives and functions after tensioning at ambient temperature.

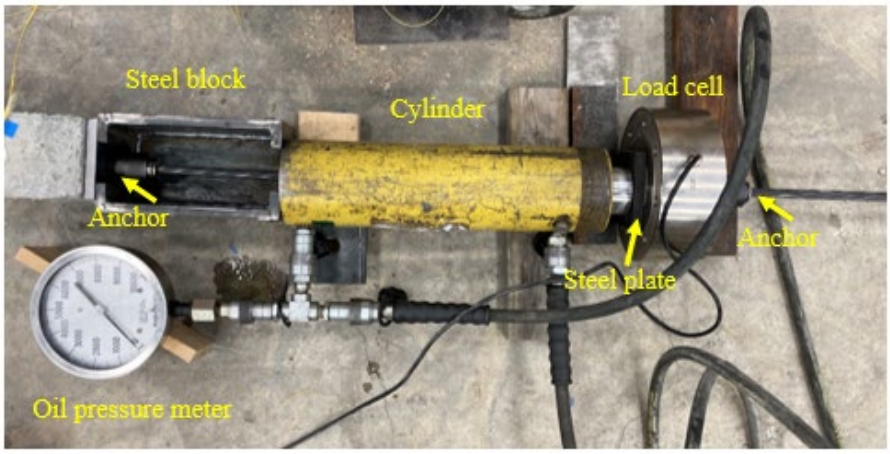

(a)

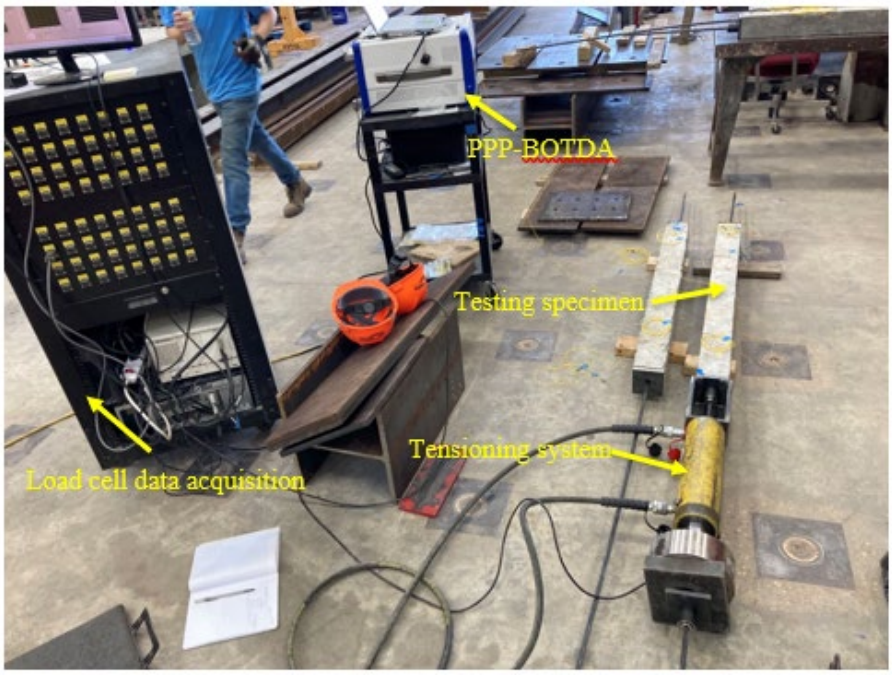

(b)

Figure 2.5 (a) New tensioning frame and (b) overall test setup.

2.3 Results and Discussion

2.3.1 Cable force during tensioning process

As mentioned in Section 2.4, distributed fiber optic sensing measurements were performed at each load step during the tensioning process. The load level applied was also

recorded by the load cell. Two distributed fiber optic strain sensors were helically bonded to the strand in each specimen. The measured results in the PPP-BOTDA data acquisition system are Brillouin frequencies. Therefore, the initial Brillouin frequency is needed as a reference for calculating the actual Brillouin frequency shift caused by the prestressing force. The initial Brillouin frequency is recorded since the value is not zero due to the epoxy shrinkage during hardening and the restraint effect provided by the strand, which can be seen in the later discussion. After the Brillouin frequency is subtracted by the initial condition value, equation (2.1) will be used to convert the frequency shift to the strain of the optical fiber. The second term in equation (2.1) is neglected due to a constant temperature environment in the Highbay lab at Missouri S&T, USA. Here, it is assumed that the strain transfer between the optical fiber and the steel strand is perfect because the two-part epoxy was used for bonding the optical fiber to the strand (Gao et al. 2006). Therefore, the strain obtained from the optical fiber can be regarded as the strand strain. As the optical fiber was bonded to the strand at the valley along the outer wires, the strain calculated from equation (2.1) is an average strain of the adjacent two wire strains. Based on this discussion, the method for calculating the prestressing force is provided as follows, which has been used in the studies from Briere et al. (2013) and Moon et al. (2010). Equations (2.2) and (2.3) show formulas for prestressing force calculation with lay angle:

$$\varepsilon_c = \frac{1}{cos^2\beta}\varepsilon_h \tag{2.2}$$

$$f_p = A_p \times \varepsilon_c \times E_p \tag{2.3}$$

where, ε_c is the strain of the center; ε_h is the strain of the helical wires and β is the lay angle as shown in Figure 2.6. The strain of the helical wires (ε_h) is measured strain from the optical fiber. Different strain statistics can be chosen to calculate the prestressing force for

comparison purposes because the strain distribution along the strand was obtained, which highlights the technical advantage of distributed fiber optic sensing in data collection. For example, average strain, maximum strain, and minimum strain from the strain distribution along the strand can be used as the strain of the helical wires (ε_h). By comparing the calculated prestressing forces with the load cell values, the errors between them can be identified, and the distributed sensing effectiveness to monitor prestressing force is examined, which is also the aim of the present study. In the following subsections, the measured and calculated results (strain and force) are presented for each specimen. Because many data were obtained from the distributed sensing, it is not ideal to combine them together to reduce analysis complexity.

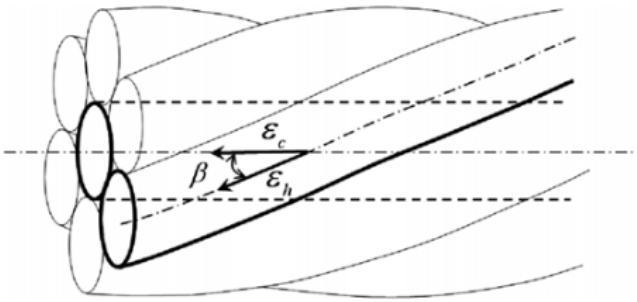

Figure 2.6 Strain relationship and lay angle (Moon et al. 2010).

2.3.1.1 PC1 Specimen

Figure 2.7 shows applied force history measured by the load cell, strain distributions along the strand, as well as calculated prestressing forces for PC1. There are six load steps as can be observed in Figure 2.7(a) and the initial load step was not recorded for the first specimen. As the force was applied by the jack cylinder, the force monitored by the load cell cannot maintain a stable and constant value after the target force value reached at each step. The target force gradually decreased as seen in Figure 2.7(a). Therefore, the values written on Figure 2.7(a)

represent average forces during each load step when the distributed sensing measurements were performed. Figure 2.7(b) and (c) shows the measured strain distributions along the outer wires of the strand, representing two instrumented optical fibers (namely, W1 and W). However, the W optical fiber only has the initial value and strain distribution after release of the force. Generally, the strain distributions along the wires at each load step are uniform, and a strain gradient can be seen at the two ends, which may be attributed to the strain transfer at the ends. Also, the repeatability for two-time measurements at each step is acceptable. The maximum strain measured by the DFOS is about 6000 $\mu\varepsilon$ and the strain after the force release is about 4000 $\mu\varepsilon$. Figure 2.7(d) shows a comparison of applied force obtained for different measurement systems. The force from the oil pressure meter is calculated by the meter reading multiplied by the effective contact area of the cylinder, while the DFOS forces are obtained by the average strain, maximum strain, or minimum strain (i.e., distance from 3.255 m to 3.942 m for the W1) multiplied by the material properties and geometrical angle of the strand. The oil pressure meter does not have readable values at the first two steps, while the load cell has an initial value of 0.205 kN. At the third step, the pressure meter only measured the force of 6.423 kN, which is much smaller than the load cell and DFOS values of 15.191 kN and 10.347 kN (from W1 average strain; the same source used for following comparisons) probably because the gaps in the test setup and manual reading of the pressure meter. At the fourth and fifth steps, the three values are approaching (i.e., 58.878 kN, 54.597 kN, and 57.741 kN at the fourth step as well as 124.340 kN, 128.464 kN, and 116.364 kN at the fifth step for load cell, pressure meter and DFOS, respectively). Overall, the three values have a good consistency. For all DFOS values, they are smaller than the load cell values because the strain transfer between the optical fiber and strand may exist. Another reason is that the center wire of the strand has a higher strain than

outer wires in the strand axis direction (Onur 2016). In the present calculation, the latter is used for calculating cable force. For the prestress loss calculated from the DFOS after the force release in PC1, the actual average prestressing force value (from W1 average strain) is 81.000 kN, which is reduced by 30.4% compared to the last step. This instant prestress loss was probably due to the gap between the specimen end and the steel plate (about 1 mm for PC1), the epoxy deformation, and concrete elastic deformation. Therefore, two improvement methods for reducing prestress loss are proposed. The first is to improve the final tensioning force, but attention should be paid to the end compression zone during force release. Although the force after prestress loss applied on the concrete specimen is usually acceptable, the sudden impact effect of the large tension force during force release (less than 10 seconds) on the concrete specimen needs attention. The second is to improve anchoring quality. In this study, increasing hitting times for the tensioning anchor before force release is beneficial. Also, trying to reduce the gap among the anchor, specimen, and end steel plate, as well as to align more perfectly between the cylinder and concrete specimen will be helpful.

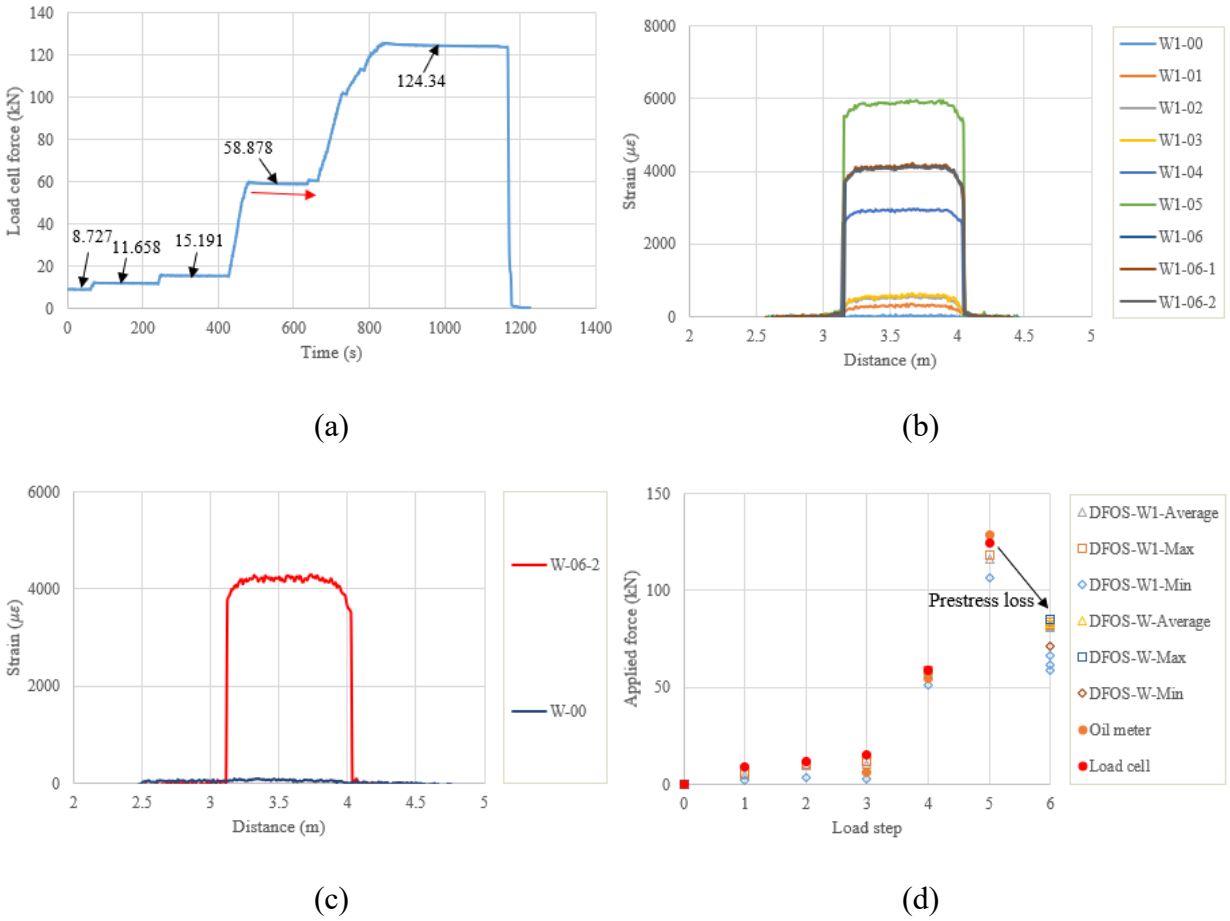

Figure 2.7 (a) Calibrated load cell readings for PC1; strain distribution along the strand (b) one strain fiber (W1); (c) the other fiber (W); (d) applied force changes at different load steps.

Table 2.4 lists a quantitative comparison between the measured and calculated forces. Note that, the small initial values of the load cell and DFOS are subtracted by their readings at a specific load to obtain the applied force induced changes. The initial value of the load cell may come from the drift error, while the initial value of DFOS comes from hardening epoxy deformation as described before. The relative error is calculated by (DFOS - load cell) / (load cell) × 100%, which applies to other tables. It can be found that at the lower loads (the first three steps for PC1), the errors between them are up to 42.69%, 33.12%, and 81.15% for the DFOS-average, DFOS-max, and DFOS-min, respectively. As the applied force increases, the errors are

significantly decreased. The errors between the load cell and DFOS-max are less than 5%, while the errors for DFOS-min are about 14%. Moreover, the prestressing force can be only monitored by the DFOS after the force is released in this test setup because of the load cell availability.

Table 2.4 Prestressing force monitored by load cell and DFOS for PC1 (unit: kN).

Load step	Load cell	DFOS-average	Error (%)	DFOS-max	Error (%)	DFOS-min	Error (%)
00	0.000	0.000	0.00	0.000	0.00	0.000	0.00
01	8.727	5.001	-42.69	5.837	-33.12	2.434	-72.12
02	11.658	9.469	-18.77	10.515	-9.81	3.714	-68.14
03	15.191	10.347	-31.89	11.887	-21.75	2.863	-81.15
04	58.878	57.741	-1.93	58.670	-0.35	50.976	-13.42
05	124.340	116.364	-6.41	118.274	-4.88	106.300	-14.51
06-1	n/a	80.858	n/a	82.366	n/a	61.910	n/a
06-2	n/a	81.419	n/a	83.813	n/a	66.515	n/a
06-3	n/a	80.724	n/a	82.532	n/a	58.540	n/a
00	0.000	0.000	0.00	0.000	0.00	0.000	0.00
06-3	n/a	82.727	n/a	85.102	n/a	71.228	n/a

In the subsections, the figures and tables like Figure 2.7 and Table 2.4 are presented for the remaining specimens in accordance with the test date. Because the specimens follow almost the same tensioning and measuring procedures, general discussion and data presentation are like those in PC1. Here, the authors are trying to point out different aspects in different specimens. Figure 2.8 and Table 2.5 show the test and calculated results of the PC5 specimen. The high temperature adhesive was used for PC5, which was different from other specimens with normal ambient temperature epoxy. Also, the hammer was used for anchoring before the force release and there are four load steps. The two optical fibers were connected in one loop to reduce measurement time and the distributed strains can be plotted in one figure. In Figure 2.8(b) there are measurement peaks (i.e., less smooth in PC5), which may come from the adhesive surface cracks and make that specimen different from other measurements. This observation indicates

that the adhesive affects the final measured results, and additional analysis is warranted. From Table 2.5, the errors between the load cell and DFOS values for average and max cases in the two optical fibers are less than 10% after the second load step, while for the min case, the errors are up to about 20%. Figure 2.9 and Table 2.6 show the testing results of the PC6 specimen. For this specimen, before the hammer was used for anchoring, the applied load was increased to the target value to slightly compensate load reduction with time since the force could not be applied after the tension end chuck was tightly anchored. Also, a slight force fluctuation can be seen because the hammer hit for anchoring, and this operation did not affect the applied force prior to the force release. Moreover, a stop point is observed in Figure 2.9(a) to check alignment of the loading system during the tensioning process. Again, from Table 2.6, the errors between the DFOS measured cable forces and load cell forces are within 10% for all average and max cases. Figure 2.10 and Table 2.7 show the testing results of the PC2 specimen. It is observed in Figure 2.10(b)that the first measured DFOS values are smaller than the second ones in the second step, while the opposite trend is true for the PC6 specimen at the third step (see Figure 2.9(b)). From Table 2.7, the maximum errors for the DFOS-min case are up to about 25% except for the first load level.

Figures 2.11-14 and Tables 2.8-11 show the testing results of the remaining four specimens. To compensate instant prestress loss after the force release as well as to maintain a high prestress level in the strand, the applied force increased by 10% compared to the previous four specimens. Therefore, one more load level appears in Figure 2.11-14(a). However, the testing and calculated results presented in Figures 2.11-14 are like the previous four specimens. Obviously, after the force release, the DFOS measured higher strain levels than the previous four

specimens with lower target loads. Moreover, the force errors between the load cell and DFOS are within about 5% for the average and max cases in these four specimens.

2.3.1.2 PC5 Specimen

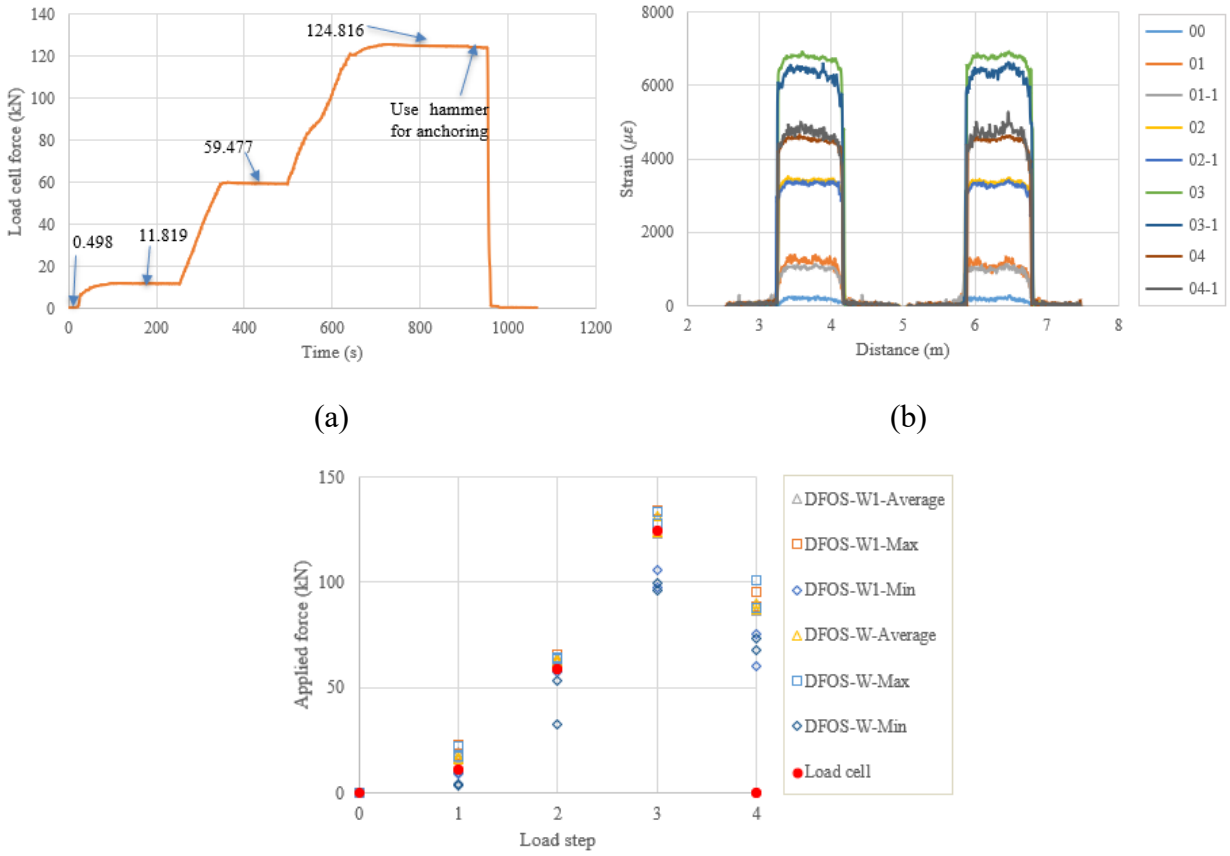

Figure 2.8 (a) Load cell readings for PC5; (b) strain distribution along the strand (W1and W fibers) (In the legend, the first number represents the load step, and the second number represents measurement times at the load step); (c) applied force changes at different load steps.

Table 2.5 Prestressing force monitored by load cell and DFOS for PC5 (unit: kN).

Load step	Load cell	DFOS-average	Error (%)	DFOS-max	Error (%)	DFOS-min	Error (%)
00	0.000	0.000	0.00	0.000	0.00	0.000	0.00
01-1	11.321	19.442	71.74	22.767	101.10	8.980	-20.68
01-2	11.321	16.558	46.26	17.765	56.92	9.970	-11.93
02-1	58.975	64.646	9.62	65.826	11.62	59.927	1.61
02-2	58.975	63.286	7.31	63.763	8.12	57.593	-2.34
03-1	124.317	131.207	5.54	134.232	7.98	97.893	-21.26
03-2	124.317	123.198	-0.90	128.209	3.13	105.955	-14.77
04-1	n/a	86.255	n/a	88.745	n/a	60.102	n/a
04-2	n/a	89.928	n/a	95.567	n/a	75.732	n/a
00	0.000	0.000	0.00	0.000	0.00	0.000	0.00
01-1	11.321	17.596	55.43	22.303	97.01	3.986	-64.79
01-2	11.321	15.802	39.58	17.219	52.10	3.548	-68.66
02-1	58.975	63.789	8.16	64.648	9.62	53.265	-9.68
02-2	58.975	62.353	5.73	63.480	7.64	48.989	-16.93
03-1	124.317	131.386	5.69	133.635	7.50	96.236	-22.59
03-2	124.317	123.519	-0.64	128.161	3.09	99.415	-20.03
04-1	n/a	86.910	n/a	87.657	n/a	73.345	n/a
04-2	n/a	90.001	n/a	100.700	n/a	67.549	n/a

2.3.1.3 PC6 Specimen

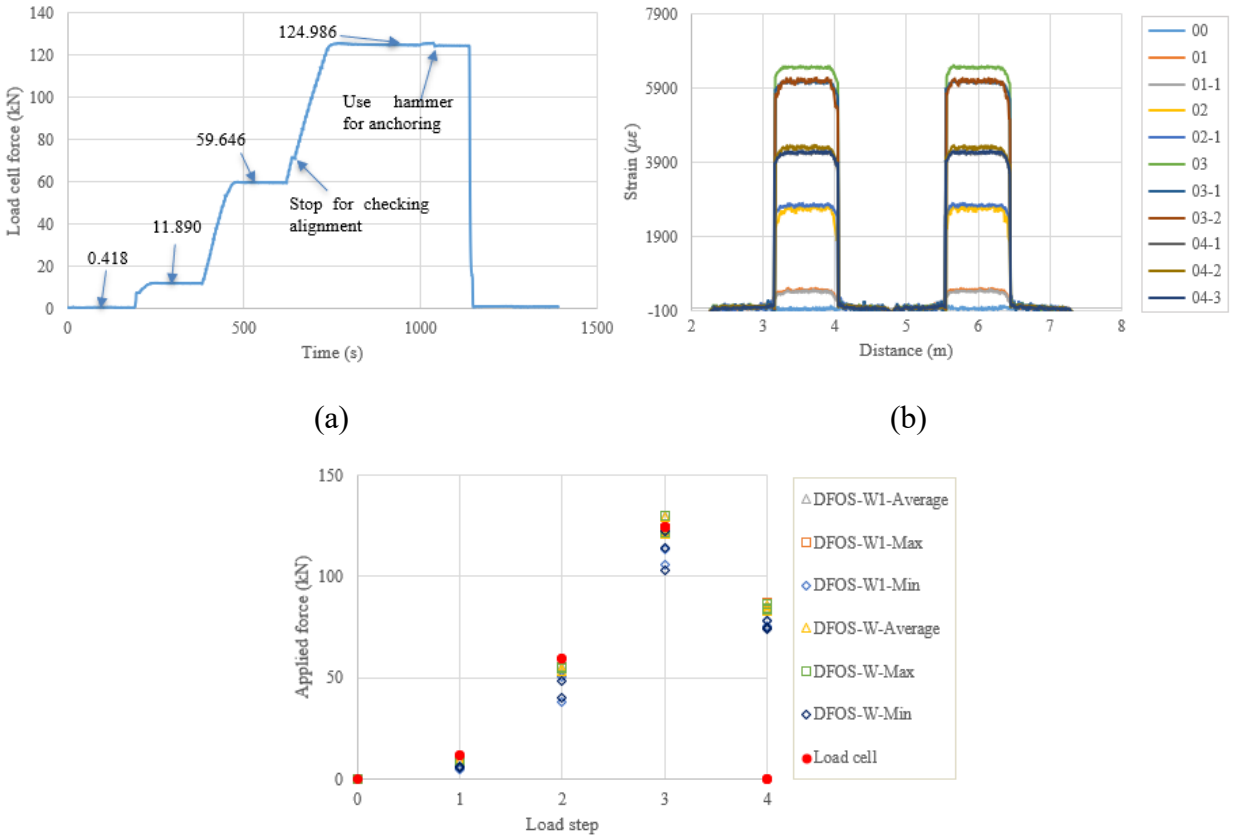

Figure 2.9 (a) Load cell readings for PC6; (b) strain distribution along the strand (W1and W fibers) (In the legend, the first number represents the load step, and the second number represents measurement times at the load step); (c) applied force changes at different load steps.

Table 2.6 Prestressing force monitored by load cell and DFOS for PC6 (unit: kN).

Load step	Load cell	DFOS-average	Error (%)	DFOS-max	Error (%)	DFOS-min	Error (%)
00	0.000	0.000	0.00	0.000	0.00	0.000	0.00
01-1	11.470	9.778	-14.75	9.954	-13.22	4.793	-58.21
01-2	11.470	8.813	-23.17	9.050	-21.09	4.831	-57.88
02-1	59.228	52.684	-11.05	55.120	-6.94	38.269	-35.39
02-2	59.228	55.129	-6.92	55.558	-6.20	50.212	-15.22
03-1	124.565	129.824	4.22	129.990	4.36	123.070	-1.20
03-2	124.565	121.955	-2.10	122.225	-1.88	113.563	-8.83
03-3	124.565	121.583	-2.39	123.618	-0.76	106.149	-14.78
04-1	n/a	84.044	n/a	84.463	n/a	74.888	n/a
04-2	n/a	86.115	n/a	87.124	n/a	75.708	n/a
04-3	n/a	83.570	n/a	83.802	n/a	78.337	n/a
00	0.000	0.000	0.00	0.000	0.00	0.000	0.00
01-1	11.470	9.715	-15.30	9.610	-16.22	6.132	-46.53
01-2	11.470	8.760	-23.63	8.866	-22.70	5.474	-52.27
02-1	59.228	53.201	-10.18	54.809	-7.46	39.973	-32.51
02-2	59.228	54.715	-7.62	55.225	-6.76	48.161	-18.68
03-1	124.565	129.527	3.98	129.883	4.27	122.171	-1.92
03-2	124.565	121.545	-2.42	121.921	-2.12	114.089	-8.41
03-3	124.565	121.325	-2.60	123.061	-1.21	103.198	-17.15
04-1	n/a	83.614	n/a	84.368	n/a	74.428	n/a
04-2	n/a	85.748	n/a	86.576	n/a	78.267	n/a
04-3	n/a	83.220	n/a	83.619	n/a	73.952	n/a

2.3.1.4 PC2 Specimen

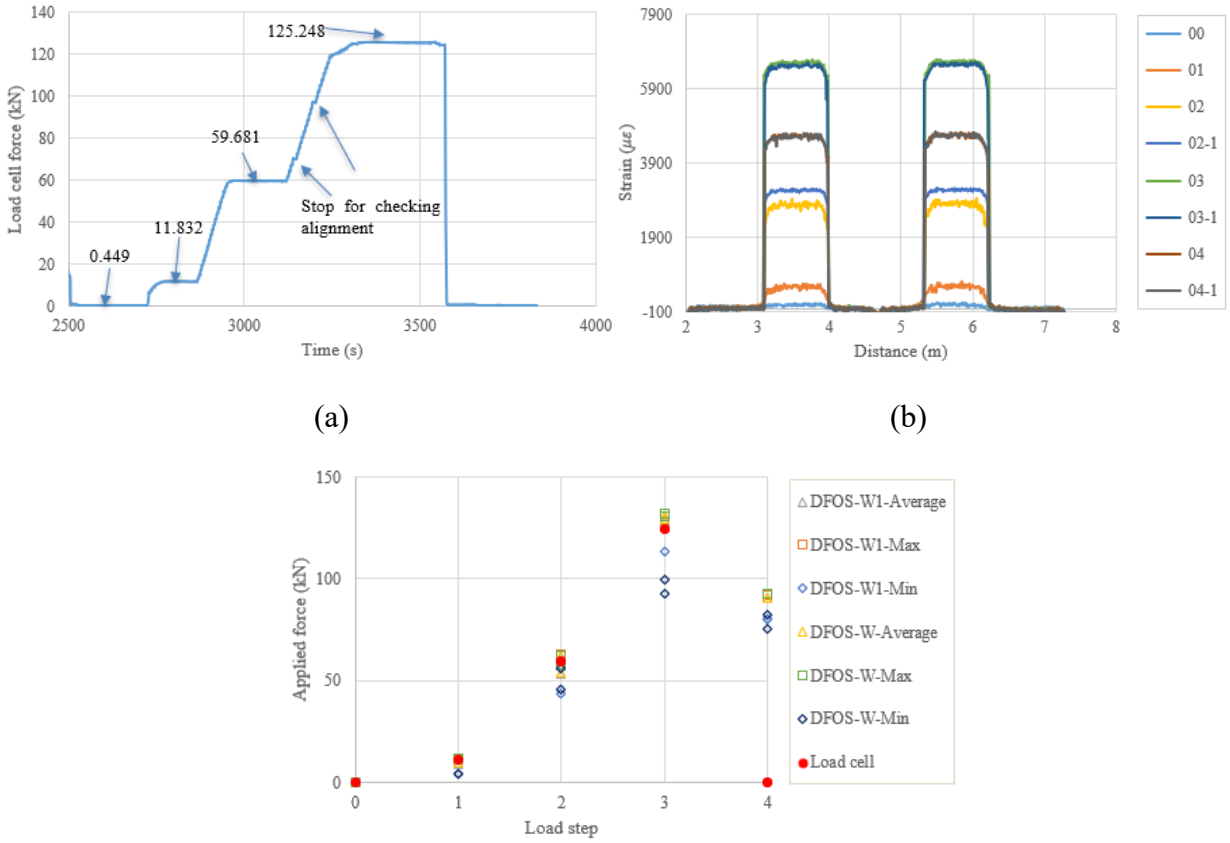

Figure 2.10 (a) Load cell readings for PC2; (b) strain distribution along the strand (W1and W fibers) (In the legend, the first number represents the load step, and the second number represents measurement times at the load step); (c) applied force changes at different load steps.

Table 2.7 Prestressing force monitored by load cell and DFOS for PC2 (unit: kN).

Load step	Load cell	DFOS-average	Error (%)	DFOS-max	Error (%)	DFOS-min	Error (%)
00	0.000	0.000	0.00	0.000	0.00	0.000	0.00
01	11.382	9.150	-19.61	10.798	-5.13	4.544	-60.08
02-1	59.231	53.503	-9.67	57.117	-3.57	43.485	-26.58
02-2	59.231	61.811	4.36	62.657	5.78	57.268	-3.31
03-1	124.798	130.694	4.72	132.112	5.86	124.189	-0.49
03-2	124.798	128.877	3.27	130.855	4.85	113.418	-9.12
04-1	n/a	90.736	n/a	92.226	n/a	80.010	n/a
04-2	n/a	90.401	n/a	92.339	n/a	80.158	n/a
00	0.000	0.000	0.00	0.000	0.00	0.000	0.00
01	11.382	9.439	-17.07	11.646	2.32	4.157	-63.47
02-1	59.231	54.073	-8.71	57.163	-3.49	45.479	-23.22
02-2	59.231	62.079	4.81	62.607	5.70	56.327	-4.90
03-1	124.798	130.545	4.61	132.029	5.79	92.752	-25.68
03-2	124.798	129.028	3.39	130.641	4.68	99.633	-20.16
04-1	n/a	90.975	n/a	92.668	n/a	75.315	n/a
04-2	n/a	90.958	n/a	93.059	n/a	82.293	n/a

2.3.1.5 PC3-1 Specimen

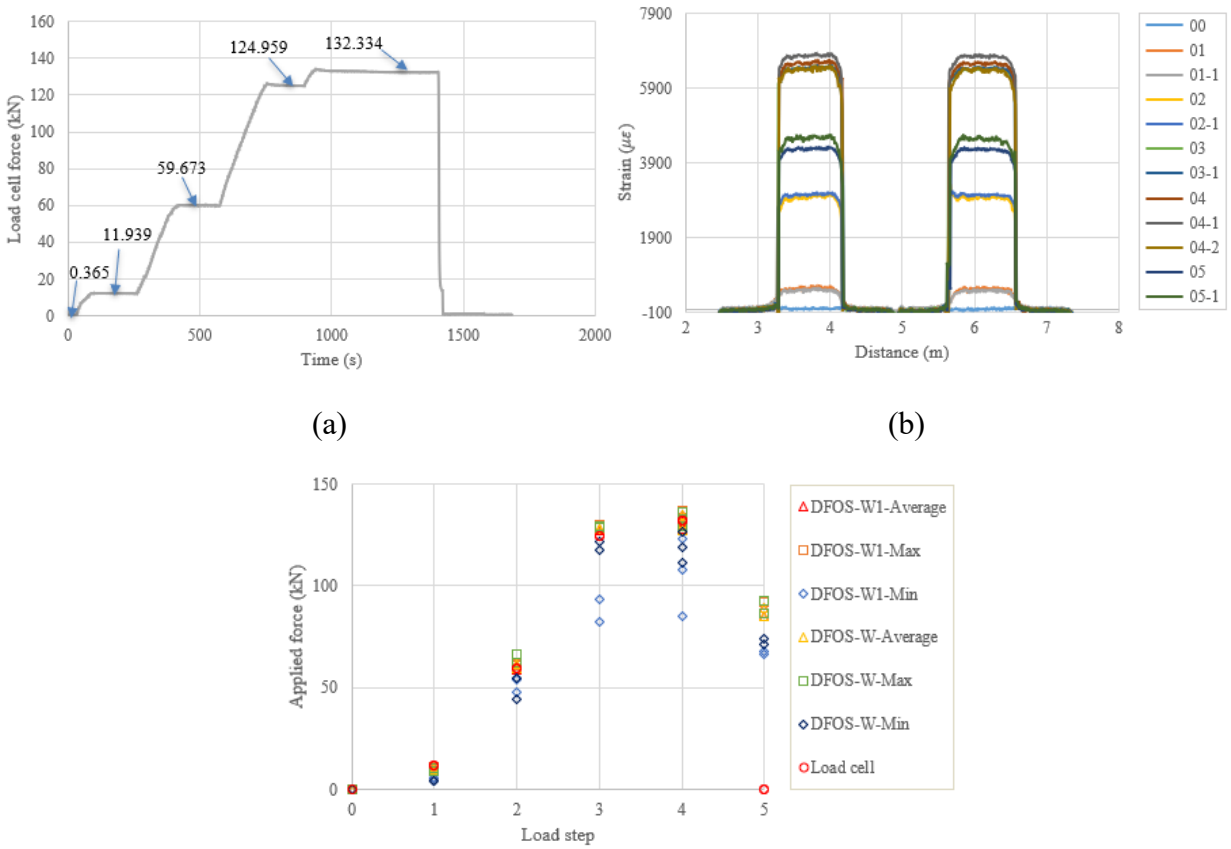

Figure 2.11 (a) Load cell readings for PC3-1; (b) strain distribution along the strand (W1and W fibers) (In the legend, the first number represents the load step, and the second number represents measurement times at the load step); (c) applied force changes at different load steps.

Table 2.8 Prestressing force monitored by load cell and DFOS for PC3-1 (unit: kN).

Load step	Load cell	DFOS-average	Error (%)	DFOS-max	Error (%)	DFOS-min	Error (%)
00	0.000	0.000	0.00	0.000	0.00	0.000	0.00
01-1	11.576	9.971	- -13.87	11.075	-4.33	5.905	- -48.99
01-2	11.576	9.007	-22.20	9.689	-16.30	5.580	-51.80
02-1	59.310	58.755	-0.94	60.802	2.52	48.038	-19.00
02-2	59.310	60.736	2.40	61.696	4.02	53.975	-9.00
03-1	124.596	127.729	2.52	130.092	4.41	93.497	-24.96
03-2	124.596	127.368	2.23	129.862	4.23	82.331	-33.92
04-1	131.969	131.521	-0.34	133.236	0.96	122.925	-6.85
04-2	131.969	134.823	2.16	136.900	3.74	85.188	-35.45
04-3	131.969	127.750	-3.20	130.275	-1.28	107.734	-18.36
05-1	n/a	85.194	n/a	86.390	n/a	68.108	n/a
05-2	n/a	89.592	n/a	92.081	n/a	66.347	n/a
00	0.000	0.000	0.00	0.000	0.00	0.000	0.00
01-1	11.576	9.694	-16.26	10.448	-9.75	4.537	-60.80
01-2	11.576	8.847	-23.58	9.330	-19.40	4.306	-62.80
02-1	59.310	59.566	0.43	66.369	11.90	44.219	-25.44
02-2	59.310	61.320	3.39	62.316	5.07	54.434	-8.22
03-1	124.596	127.729	2.52	128.928	3.48	117.508	-5.69
03-2	124.596	128.225	2.91	129.133	3.64	121.631	-2.38
04-1	131.969	131.081	-0.67	132.517	0.41	118.657	-10.09
04-2	131.969	135.008	2.30	136.341	3.31	126.597	-4.07
04-3	131.969	127.023	-3.75	129.567	-1.82	111.366	-15.61
05-1	n/a	85.028	n/a	86.403	n/a	74.242	n/a
05-2	n/a	89.335	n/a	92.386	n/a	71.173	n/a

2.3.1.6 PC3-2 Specimen

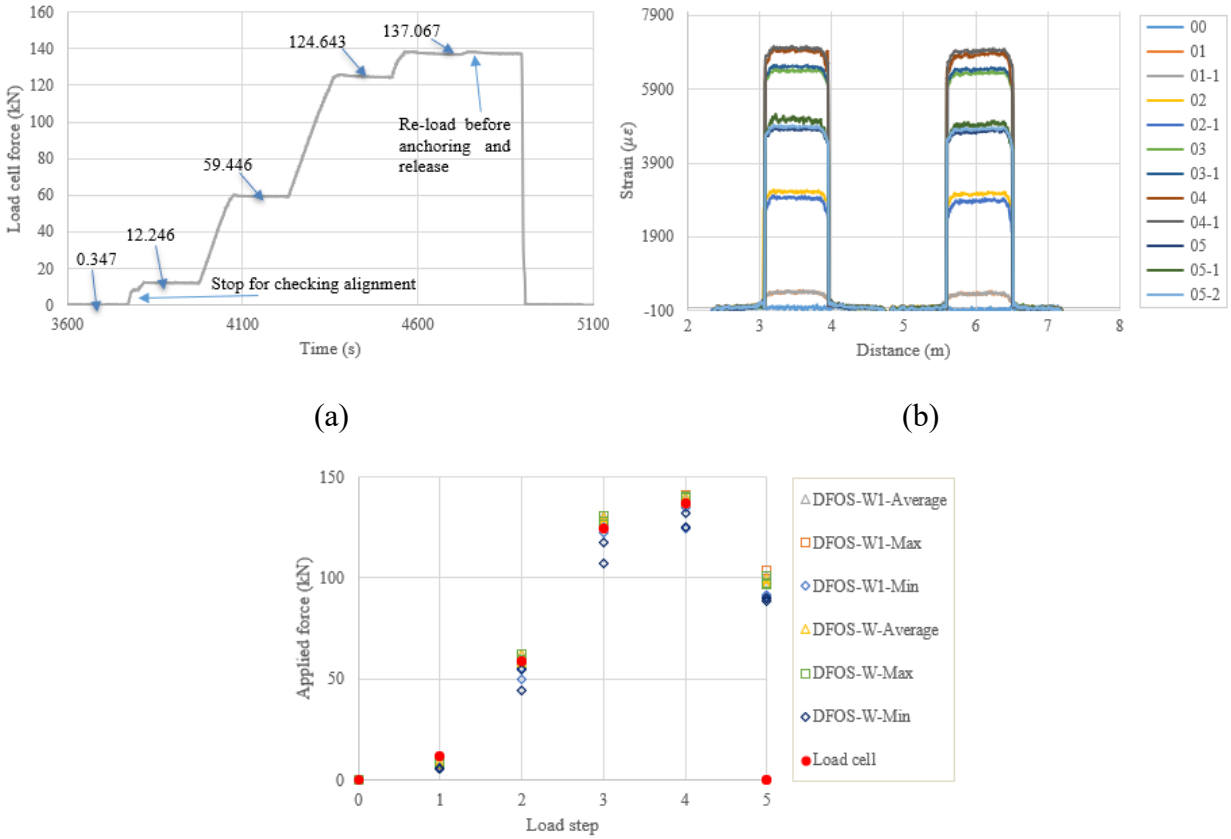

Figure 2.12 (a) Load cell readings for PC3-2; (b) strain distribution along the strand (W1and W fibers) (In the legend, the first number represents the load step, and the second number represents measurement times at the load step); (c) applied force changes at different load steps.

Table 2.9 Prestressing force monitored by load cell and DFOS for PC3-2 (unit: kN).

Load step	Load cell	DFOS-average	Error (%)	DFOS-max	Error (%)	DFOS-min	Error (%)
00	0.000	0.000	0.00	0.000	0.00	0.000	0.00
01-1	11.901	7.856	-33.98	7.778	-34.64	6.277	-47.26
01-2	11.901	8.167	-31.37	7.992	-32.85	6.109	-48.66
02-1	59.101	62.171	5.19	62.310	5.43	55.481	-6.13
02-2	59.101	58.867	-0.40	59.752	1.10	49.959	-15.47
03-1	124.296	128.155	3.10	128.271	3.20	122.666	-1.31
03-2	124.296	130.625	5.09	130.840	5.26	125.277	0.79
04-1	136.722	139.230	1.83	139.844	2.28	124.369	-9.04
04-2	136.722	140.397	2.69	140.861	3.03	134.637	-1.52
05-1	n/a	96.833	n/a	97.022	n/a	91.201	n/a
05-2	n/a	100.908	n/a	103.849	n/a	91.518	n/a
05-3	n/a	97.519	n/a	97.767	n/a	91.275	n/a
00	0.000	0.000	0.00	0.000	0.00	0.000	0.00
01-1	11.901	8.261	-30.58	8.604	-27.70	5.253	-55.86
01-2	11.901	8.534	-28.29	8.191	-31.17	5.653	-52.50
02-1	59.101	62.172	5.20	62.381	5.55	54.573	-7.66
02-2	59.101	58.101	-1.69	59.249	0.25	44.358	-24.94
03-1	124.296	127.818	2.83	128.181	3.13	117.758	-5.26
03-2	124.296	130.114	4.68	130.546	5.03	107.454	-13.55
04-1	136.722	137.864	0.84	139.582	2.09	125.185	-8.44
04-2	136.722	140.098	2.47	140.486	2.75	131.847	-3.57
05-1	n/a	96.690	n/a	96.889	n/a	90.255	n/a
05-2	n/a	99.559	n/a	101.081	n/a	89.953	n/a
05-3	n/a	97.331	n/a	97.415	n/a	88.762	n/a

2.3.1.7 PC4-1 Specimen

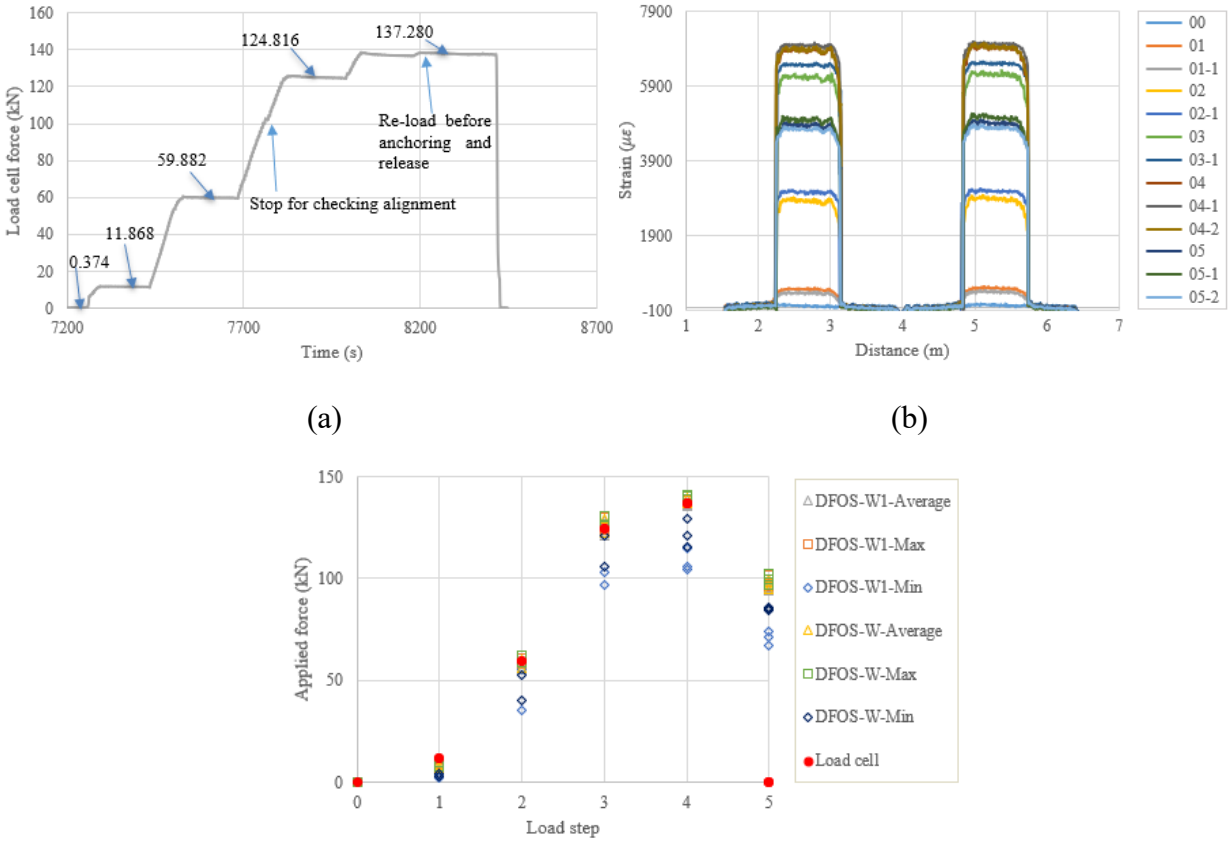

Figure 2.13 (a) Load cell readings for PC4-1; (b) strain distribution along the strand (W1and W fibers) (In the legend, the first number represents the load step, and the second number represents measurement times at the load step); (c) applied force changes at different load steps.

Table 2.10 Prestressing force monitored by load cell and DFOS for PC4-1 (unit: kN).

Load step	Load cell	DFOS-average	Error (%)	DFOS-max	Error (%)	DFOS-min	Error (%)
00	0.000	0.000	0.00	0.000	0.00	0.000	0.00
01-1	11.493	8.443	-26.54	8.822	-23.25	3.251	-71.72
01-2	11.493	6.530	-43.18	7.211	-37.26	1.927	-83.23
02-1	59.508	55.142	-7.34	57.827	-2.83	35.350	-40.60
02-2	59.508	60.493	1.65	61.206	2.85	55.365	-6.96
03-1	124.446	121.118	-2.67	124.099	-0.28	96.900	-22.13
03-2	124.446	128.895	3.58	130.266	4.68	102.899	-17.31
04-1	136.906	135.695	-0.88	138.568	1.21	104.218	-23.88
04-2	136.906	139.205	1.68	140.460	2.60	115.004	-16.00
04-3	136.906	136.206	-0.51	139.053	1.57	105.520	-22.92
05-1	n/a	95.657	n/a	97.962	n/a	71.612	n/a
05-2	n/a	98.979	n/a	101.689	n/a	73.822	n/a
05-3	n/a	94.209	n/a	96.033	n/a	67.085	n/a
00	0.000	0.000	0.00	0.000	0.00	0.000	0.00
01-1	11.493	8.601	-25.17	9.566	-16.77	4.360	-62.06
01-2	11.493	6.738	-41.38	7.461	-35.08	2.929	-74.52
02-1	59.508	55.741	-6.33	58.660	-1.43	39.918	-32.92
02-2	59.508	60.332	1.38	61.975	4.15	52.926	-11.06
03-1	124.446	122.215	-1.79	125.573	0.91	105.557	-15.18
03-2	124.446	129.420	4.00	130.457	4.83	120.906	-2.84
04-1	136.906	136.909	0.00	139.267	1.72	120.852	-11.73
04-2	136.906	139.613	1.98	141.103	3.07	129.390	-5.49
04-3	136.906	137.287	0.28	140.571	2.68	115.665	-15.52
05-1	n/a	96.637	n/a	99.383	n/a	84.826	n/a
05-2	n/a	99.644	n/a	102.654	n/a	84.301	n/a
05-3	n/a	94.752	n/a	96.981	n/a	85.673	n/a

2.3.1.8 PC4-2 Specimen

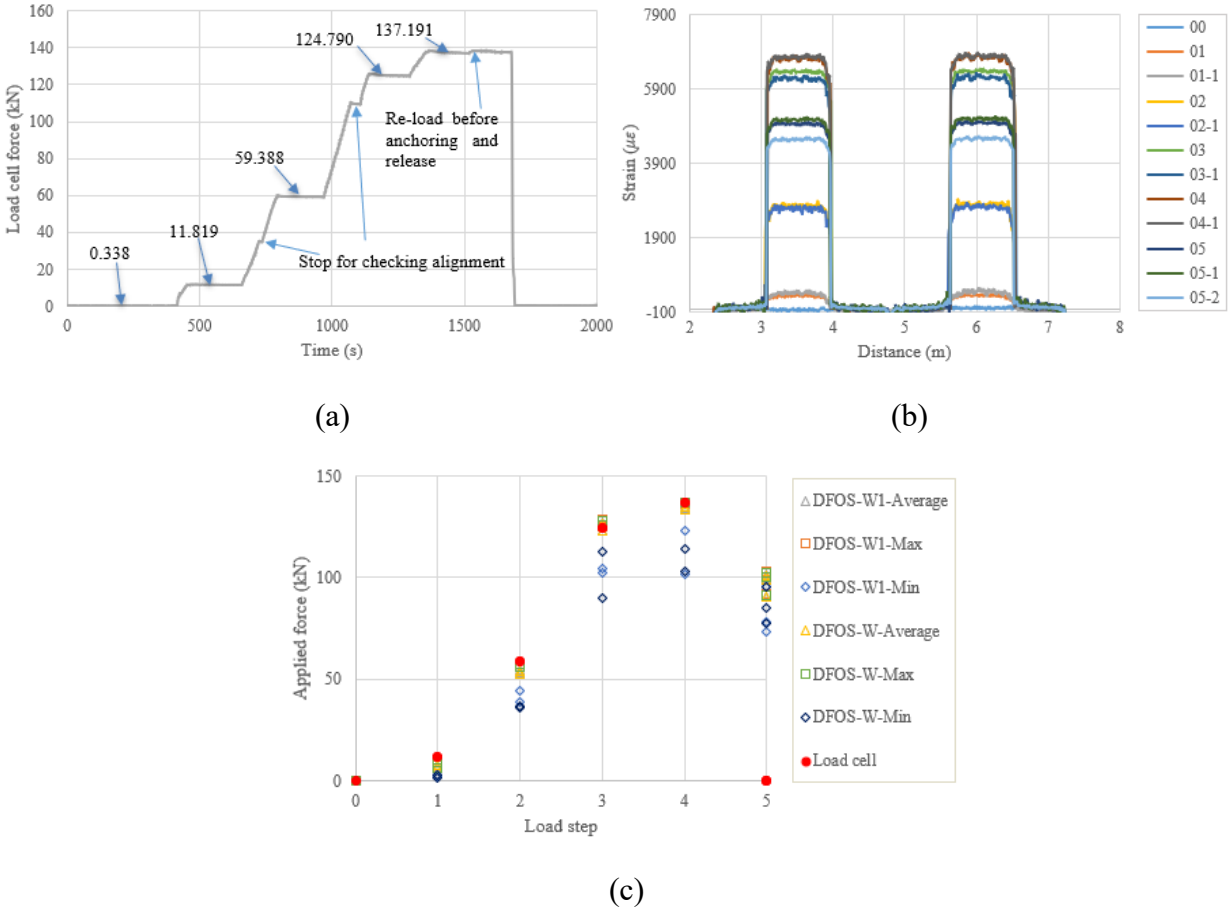

Figure 2.14 (a) Load cell readings for PC4-2; (b) strain distribution along the strand (W1and W fibers) (In the legend, the first number represents the load step, and the second number represents measurement times at the load step); (c) applied force changes at different load steps.

Table 2.11 Prestressing force monitored by load cell and DFOS for PC4-2 (unit: kN).

Load step	Load cell	DFOS-average	Error (%)	DFOS-max	Error (%)	DFOS-min	Error (%)
00	0.000	0.000	0.00	0.000	0.00	0.000	0.00
01-1	11.478	6.778	-40.95	7.475	-34.87	2.567	-77.64
01-2	11.478	7.767	-32.34	8.902	-22.44	2.328	-79.72
02-1	59.051	54.666	-7.43	57.674	-2.33	44.315	-24.95
02-2	59.051	53.455	-9.48	55.740	-5.61	38.914	-34.10
03-1	124.451	127.394	2.37	128.788	3.49	102.470	-17.66
03-2	124.451	123.359	-0.88	125.285	0.67	104.631	-15.93
04-1	136.853	134.335	-1.84	136.297	-0.41	122.983	-10.14
04-2	136.853	134.899	-1.43	137.109	0.19	101.760	-25.64
05-1	n/a	99.606	n/a	100.636	n/a	73.579	n/a
05-2	n/a	101.721	n/a	102.959	n/a	95.737	n/a
05-3	n/a	90.972	n/a	91.713	n/a	78.140	n/a
00	0.000	0.000	0.00	0.000	0.00	0.000	0.00
01-1	11.478	5.988	-47.83	6.562	-42.83	2.729	-76.22
01-2	11.478	7.408	-35.47	9.292	-19.05	1.549	-86.50
02-1	59.051	54.246	-8.14	57.732	-2.23	36.300	-38.53
02-2	59.051	52.863	-10.48	55.910	-5.32	36.627	-37.97
03-1	124.451	126.666	1.78	128.316	3.11	90.153	-27.56
03-2	124.451	123.117	-1.07	125.757	1.05	112.596	-9.53
04-1	136.853	133.648	-2.34	136.684	-0.12	102.903	-24.81
04-2	136.853	134.723	-1.56	136.714	-0.10	114.171	-16.57
05-1	n/a	99.201	n/a	100.586	n/a	77.373	n/a
05-2	n/a	101.354	n/a	102.400	n/a	95.209	n/a
05-3	n/a	90.596	n/a	91.363	n/a	85.452	n/a

2.3.2 Linear regression analysis

The aim of the present study is to use DFOS for monitoring the prestressing force in the cable. If a simple and direct relationship between the prestressing force and the measured quantities can be established, the DFOS assisted cable force monitoring will have a more solid basis to promote its application in engineering structures. Based on a lot of data obtained from DFOS in different specimens, the regression analysis can be a mathematical tool to investigate the relation between the ground truth cable force and DFOS strain (or calculated force). Here, the prestressing force in the cable from the load cell can be a dependent variable, while the independent variable can be DFOS strain (or calculated force). Because only one independent variable exists, a linear regression model can be used to establish their relationship. The least

square method is usually used to obtain a theoretical prediction equation describing this relationship. The principle of the least square method is to minimize the sum of squared residuals.

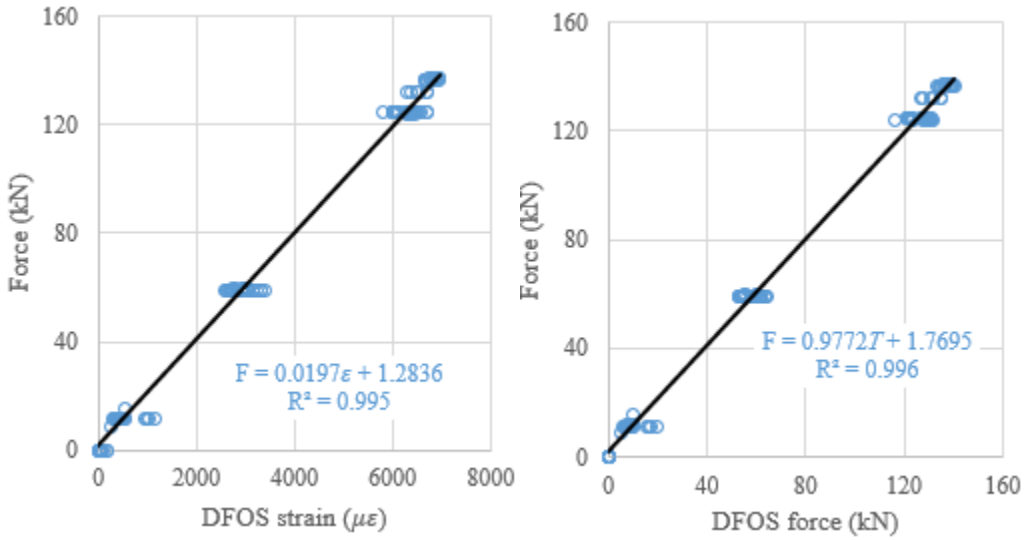

(a) (b)

Figure 2.15 (a) Prestressing force versus DFOS average strain; (b) prestressing force versus DFOS average strain calculated force.

When the DFOS average strain integrated from the strain distribution along the strand or the DFOS average strain-calculated force was used as an independent variable to predict the prestressing force (as a dependent variable), the theoretical prediction equations found using the least square method are written on Figure 2.15(a) and (b). Moreover, to verify the effectiveness of the theoretical prediction equations, the determination coefficients (R2) are reported in Figure 2.15. It is found that the R2 are 0.995 for the average strain case and 0.996 for the average strain calculated force case. Therefore, the measured strain from DFOS shows a strong correlation with the load cell force (i.e., ground truth) because the determination coefficients approach 1. The

same procedures are applied to the relations between the DFOS-max strain and cable force or between the DFOS-min strain and cable force. For the max strain and the max strain-calculated force as independent variables, the R2 are 0.994 and 0.996 as shown in Figure 2.16, respectively. For the min strain and the min strain-based force as independent variables, the R2 are 0.971 and 0.970 as shown in Figure 2.17, respectively. Also, it is observed that the line slopes in Figures 2.15(b) and Figure 2.16(b) are less than 1, and less than the line slope in Figure 2.17(b). All residual terms in the fitted equations are small and the residual terms in Figures 2.15 and 2.16 are smaller than 2 kN.

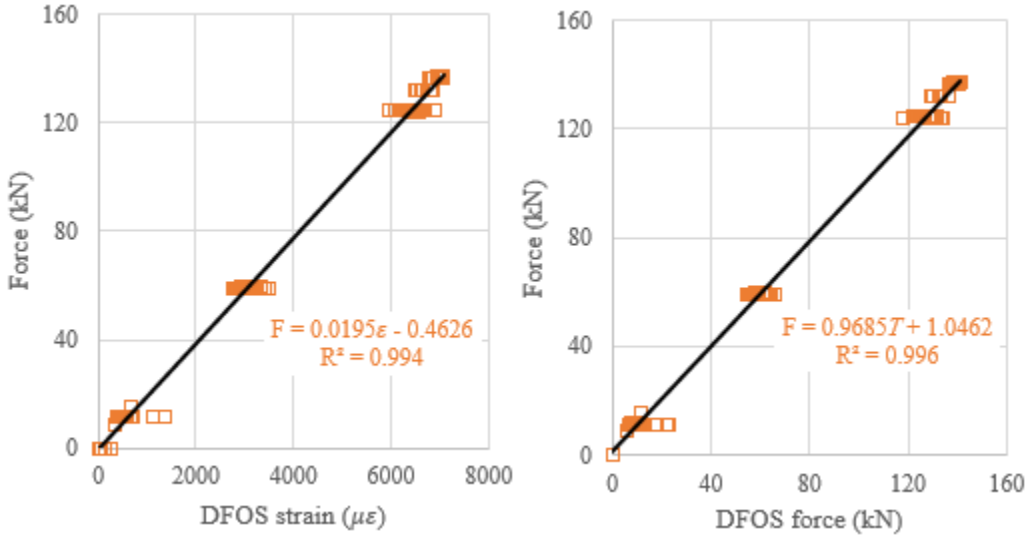

(a) (b)

Figure 2.16 (a) Prestressing force versus DFOS max strain; (b) prestressing force versus DFOS max strain calculated force.

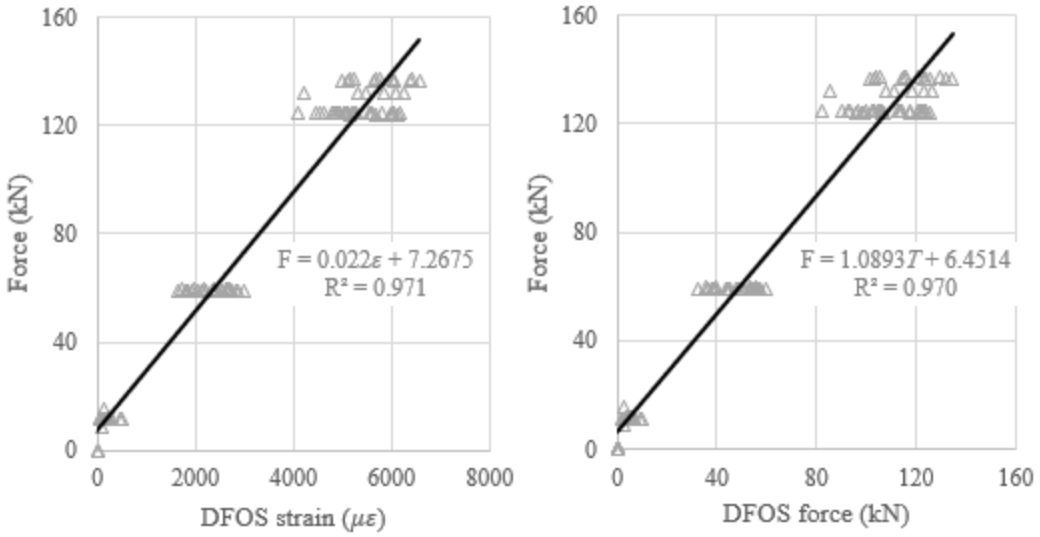

(a) (b)

Figure 2.17 (a) Prestressing force versus DFOS min strain; (b) prestressing force versus DFOS min strain calculated force.

2.3.3 Instant prestress loss

In this test setup, the load cell cannot monitor the prestressing force after the force release. The DFOS provides useful strain data to quantify the instant prestress loss due to the anchor retraction, end steel plate and epoxy deformation, and elastic deformation of the concrete specimen. As the DFOS strain or DFOS strain calculated force has a linear relationship with the cable force as discussed in Section 3.2, the prestress loss percentage can be determined by the strain calculated force change before and after the force release, which means that it is not necessary to know the actual cable force if only the prestress loss percentage is required. However, the actual cable force after the force release can be calculated by the linear equations as shown in Figures 2.15-17. To obtain the prestress loss percentage, the data in Tables 2.4-11 can be used. Here, the last-time DFOS measurement before the force release is regarded as the reference value. Then, the instant prestress loss percentage is calculated by (the reference value -

DFOS measured force after force release) / the reference value × 100%. Some specimens had two-time DFOS measurements, and some specimens had three-time DFOS measurements. Moreover, for each specimen, there were two optic fibers (except for PC1) and three statistics (i.e., average strain, max strain, and min strain) used to calculate DFOS measured forces. Therefore, fifteen legends and three regions can be seen in Figure 2.18. Obviously, the scatter of prestress loss percentages can be observed for different DFOS strain calculated forces. The greatest scatter comes from DFOS-min strain, followed by DFOS-max strain and DFOS average strain. For the average and max cases, the prestress loss percentages are within 25%-35% in this test setup. For example, if the target prestressing force is 65% of the ultimate strength of the steel strand, the remaining prestress level will be 45.5% after force release with a prestress loss percentage of 30% (which is the case for PC1); for PC2, after the instant prestress loss, the prestress level can be up to 51.6%.

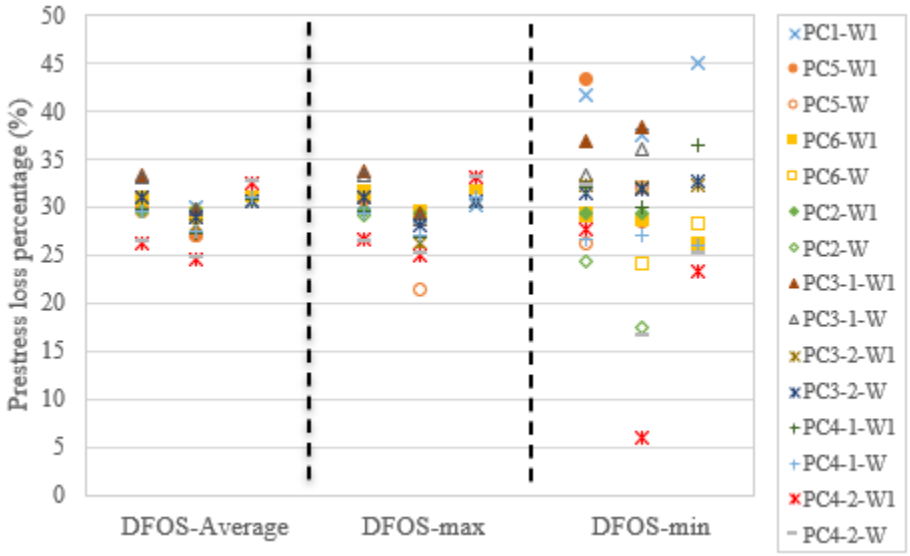

Figure 2.18 Prestress loss percentage for all specimens in the present test setup**.**

2.4 Summary

The present study proposes a spiral deployment scheme of Brillouin scattering-based DFOS to measure prestressing forces of the cables in the concrete bars post-tensioned in a custom-built test setup and to replace loading cells with a more complicated installation and less availability. The DFOS were helically bonded to the steel strand along the valley between the adjacent two outer wires. All DFOS survived during the tensioning process (up to 75% of the ultimate strength of the steel strand) after releasing the force and strain distributions along the strand were obtainable from the strain-frequency coefficient. After considering the bonded DFOS direction along with the material properties of the strand, the cable forces can be calculated at different load levels. With strain distribution along the strand, three statistics (i.e., DFOS-average strain, DFOS-maximum strain, and DFOS-minimum strain) were used to calculate cable forces. Comparing DFOS measured cable forces (including average, max, and min) with load cell values (and oil pressure meter values for PC1 specimen only), the relative errors between them at small load levels (less than 12 kN) were high (more than 50%), while the relative errors were smaller than about 10% after the second load level, even 5% for the average and max cases in some specimens. For the three cases (i.e., average, max, and min), the relations between the DFOS measured strains (or calculated forces) and the load cell forces were established. All of them showed good linearity with the minimum determination coefficient of 0.970 in the min case; the residual terms were smaller than 2 kN in the average and max cases. Moreover, based on the test DFOS results before and after force release, the instant prestress loss percentages for the three cases were calculated. The most evident scatter was observed in the min case, while about 30% instant prestress loss percentage can be determined from the average and max cases for the present test setup. Also, it is found that the epoxy type may have significant

effect on the measured cable forces, which warrants further investigation. The epoxy construction procedure may induce optical fiber position uncertainty and void defect near the bottom triangle region. One approach potentially solving the void defect is that one-thin-layer epoxy is put at the valley first as a cushion layer and the optical fiber is placed as the present procedure, then the second-layer epoxy covers at the top. However, robot-assisted automatic construction is still desired to reduce optical fiber position uncertainty in the future. Moreover, the strain transfer from the steel wires to the optical fiber deserves further investigations since two steel wires are involved in this strain transfer and the steel wires have a spiral shape in space, which are different from the traditional strain transfer case.

Chapter 3 Conclusions

In the present study, experimental studies were performed to investigate the feasibility of strain and temperature measurements of concrete and prestressed concrete structures at ambient or high temperatures using Brillouin scattering-based distributed fiber optic sensors.

The first study aims to characterize the effects of multilayered coatings on the performance of distributed fiber optic sensors (DFOS) when the coatings experience softening and melting at high temperatures. Two strain sensors (B-DFOS and W-DFOS) and one temperature sensor (Y-DFOS) were calibrated and either embedded along the centerline of a mortar bar or bonded on the surface of the specimen. The Y-DFOS was found to be no longer strain-free at high temperatures since the softened sheath, aramid yarns, buffer, and polymer coatings became viscous and adhered to their surrounding mortar above softening temperatures, i.e., 263-320 ℃. Both the B-DFOS and W-DFOS captured uneven strain distributions along the mortar specimen due to nonuniform temperature distribution, mortar heterogeneity, and strain transfer efficiency. The W-DFOS showed higher measured strains than the calculated thermal-induced strains at 100 ℃ - 300 ℃ due to the high thermal expansion coefficient of the additional buffer. The B-DFOS gave smaller measured strains than the thermal-induced strains at 300 ℃ - 500 ℃. The displacement calculated by integrating the measured strains along the length of each mortar specimen was related to the applied temperature by parabolic regression equations. The present study explores the potential use of distributed fiber optic sensors for measuring strain and temperature distributions in mortar and concrete structures at high temperatures.

On-time monitoring and condition assessment of steel cables provide mission-critical data for informed decision-making, ensuring the structural safety of post-tensioned concrete structures. This study aims to develop a spiral deployment scheme of distributed fiber optic

sensors (DFOSs) and monitor/assess the post-tensioned force in 7-wire twisted steel cables based on a pulse-pre-pump Brillouin optical time domain analysis. Each DFOS was placed in a spiral shape between two surface wires of a steel cable and glued to the steel cable by epoxy. Image observations were conducted to investigate the bonding condition between the optical fiber and the steel wires. Eight concrete bar specimens were cast, each with a pre-embedded plastic or metal duct at its center, and post-tensioned by a steel strand through the duct once instrumented with two strain and two temperature sensors. The strand was loaded/unloaded and monitored by measuring the Brillouin frequency shifts and correlating them with the applied strains and resulting cable force after temperature compensation. The maximum, minimum, and average cable forces integrated from the measured stain data were compared and validated with those from a load cell. The maximum (or average) cable force was linearly related to the ground truth data with a less than 10% error between them after any initial slack had been removed from the test setup. The post-tensioned force loss was bounded by approximately 30% using the test setup designed in the second study.

References

Abdel-Jaber, H., and B. Glisic, 2019a. “Monitoring of long-term prestress losses in prestressed concrete structures using fiber optic sensors.” *Structural Health Monitoring*. 18, 254–269.

Abdel-Jaber, H., and B. Glisic, 2019b. “Monitoring of prestressing forces in prestressed concrete structures—An overview.” *Structural Control and Health Monitoring*. 26, 1–27.

Bao, Y., and G. Chen, 2015. “Strain distribution and crack detection in thin unbonded concrete pavement overlays with fully distributed fiber optic sensors.” *Optical Engineering*. 55, 011008.

Bao, Y., and G. Chen, 2016a. “Temperature-dependent strain and temperature sensitivities of fused silica single mode fiber sensors with pulse pre-pump Brillouin optical time domain analysis.” *Measurement Science and Technology*. 27, 065101.

Bao, Y., and G. Chen, 2016b. “High-temperature measurement with Brillouin optical time domain analysis of an annealed fused-silica single-mode fiber.” *Optics Letters*. 41; 3177–3180.

Bao, Y., F. Tang, Y. Chen, W. Meng, Y. Huang, and G. Chen, 2016. “Concrete pavement monitoring with PPP-BOTDA distributed strain and crack sensors.” *Smart Structures and Systems*. 18; 405–423.

Bao, Y., M. Hoehler, C. M. Smith, and G. Chen, 2017a. “Temperature measurement and damage detection in concrete beams exposed to fire using PPP-BOTDA based fiber optic sensors.” *Smart Materials and Structures*. 26, 105034.

Bao, Y., M. S. Hoehler, C. M. Smith, M. Bundy, and G. Chen, 2020. “Measuring three-dimensional temperature distributions in steel–concrete composite slabs subjected to fire using distributed fiber optic sensors.” *Sensors*. 20, 5518.

Bao, Y., M. Valipour, W. Meng, K. H. Khayat, and G. Chen, 2017a. “Distributed fiber optic sensor-enhanced detection and prediction of shrinkage-induced delamination of ultra-high-performance concrete overlay.” *Smart Materials and Structures*. 26, 085009.

Bao, Y., Y. Chen, M. S. Hoehler, C. M. Smith, M. Bundy, and G. Chen, 2017b. “Experimental analysis of steel beams subjected to fire enhanced by Brillouin scattering-based fiber optic sensor data.” *Journal of Structural Engineering*. 143, 04016143.

Blaine, R. L., 2022. “TA123: Determination of polymer crystallinity by differential scanning calorimetry (DSC).” *TA Instruments*, New Castle, DE. File:///C:/Users/gchen/Documents/paper/Journal%20Papers/TA123new.pdf

Briere, V., K. A. Harries, J. Kasan, and C. Hager, 2013. “Dilation behavior of seven-wire prestressing strand-The Hoyer effect.” *Construction and Building Materials*. 40, 650–658.

Butler, L. J., N. Gibbons, P. He, C. Middleton, and M. Z. E. B. Elshafie, 2016. "Evaluating the early-age behaviour of full-scale prestressed concrete beams using distributed and discrete fibre optic sensors." *Construction and Building Materials*. 126, 894–912.

Cruz, C. R., 1980. "Thermal expansion of Portland cement paste, mortar and concrete at high temperatures." *Fire and Materials*. 4; 66–70.

Gao, J., B. Shi, W. Zhang, and H. Zhu, 2006. "Monitoring the stress of the post-tensioning cable using fiber optic distributed strain sensor." *Journal of the International Measurement Confederation*. 39, 420–428.

Gawin, D., F. Pesavento, and B. A. Schrefler, 2004. "Modelling of deformations of high strength concrete at elevated temperatures." *Materials and Structures*. 37; 218–236.

Gu, H., H. Dong, G. Zhang, J. He, and H. Pan, 2013. "Effects of polymer coatings on temperature sensitivity of Brillouin frequency shift within double-coated fibers." *IEEE Sensors*. Journal 13; 864-869.

Güemes, A., A. Fernández-López, and B. Soller, 2010. "Optical fiber distributed sensing - physical principles and applications." *Structural Health Monitoring*. 9, 233-245.

He, J., Z. Zhou, and J. Ou, 2013. "Optic fiber sensor-based smart bridge cable with functionality of self-sensing." *Mechanical Systems and Signal Processing*. 35, 84–94.

Huynh, T.C., and J. T. Kim, 2017. "FOS-Based Prestress Force Monitoring and Temperature Effect Estimation in Unbonded Tendons of PSC Girders." *Journal of Aerospace Engineering*. 30, 1-14.

Kim, J. M., H. W. Kim, Y. H. Park, I. H. Yang, and Y. S. Kim, 2012. "FBG sensors encapsulated into 7-wire steel strand for tension moni-toring of a prestressing tendon." *Advances in Structural Engineering*. 15, 907–917.

Kodur, V. K. R., S. Banerji, and R. Solhmirzaei, 2020. "Test methods for characterizing concrete properties at elevated temperature." *Fire and Materials*. 44; 381–395.

Lan, C., 2011. "Monitoring of structural prestress loss in RC beams by inner distributed Brillouin and fiber Bragg grating sensors on a single optical fiber." *Structural Control and Health Monitoring*.

Lan, C., Z. Zhou, and J. Ou, 2012. "Full-scale prestress loss monitoring of damaged RC structures using distributed optical fiber sensing technology." *Sensors*. 12, 5380–5394.

Le, D. B., S. D. Tran, J. L. Torero, and V. T. N. Dao, 2019. "Application of digital image correlation system for reliable deformation measurement of concrete structures at high temperatures." *Engineering Structures*. 192; 181–189.

Le, D. B., S. D. Tran, V. T. N. Dao, and J. Torero, 2017. "Deformation capturing of concrete structures at elevated temperatures." *Procedia Engineering*. 210; 613–621.

Lee, Y. W., G. Y. Kim, N. Gucunski, G. C. Choe, and M. H. Yoon, 2016. “Thermal strain behavior and strength degradation of ultra-high-strength-concrete.” *Materials and Structures*. 49; 3411–3421.

Liang, C., Q. Bai, M. Yan, Y. Wang, H. Zhang, and B. Jin, 2021. “A Comprehensive Study of Optical Frequency Domain Reflectometry.” *IEEE Access*. 9, 41647–41668.

Loser, R., B. Münch, and P. Lura, 2010. “A volumetric technique for measuring the coefficient of thermal expansion of hardening cement paste and mortar.” *Cement and Concrete Research*. 40; 1138–1147.

Lu, X., A. M. Soto, and L. Thevenaz, 2018. “Impact of the fiber coating on the temperature response of distributed optical fiber sensors at cryogenic ranges.” *Journal of Lightwave Technology*. 36; 961-967.

Meng, W., M. Valipour, and K.H. Khayat, 2017. “Optimization and performance of cost-effective ultra-high performance concrete.” *Materials and Structures*. 50, 29.

Moon, D. Y., G. Zi, J. H. Kim, S. J. Lee, and G. Kim, 2010. “On strain change of prestressing strand during detensioning procedures.” *Engineering Structures*. 32, 2570–2578.

Murayama, H., H. Igawa, K. Omichi, and Y. Machijima, 2011. “Distributed sensing with OFDR and its application to structural health monitoring Proc SPIE.” *International Society for Optical Engineering*. 7753.

Nazarian, E., F. Ansari, X. Zhang, and T. Taylor, 2016. “Detection of tension loss in cables of cable-stayed bridges by distributed mon-itoring of bridge deck strains.” *Journal of Structural Engineering*. 142, 04016018.

Novak, M. D., and F. W. Zok, 2011. “High-temperature materials testing with full-field strain measurement: Experimental design and practice.” *Review of Scientific Instruments*. 82, 115101.

Onur, Y.A., 2016. “Experimental and theoretical investigation of prestressing steel strand subjected to tensile load.” *International Journal of Mechanical Sciences*. 118, 91–100.

Pan, Z., S. Huang, Y. Su, M. Qiao, and Q. Zhang, 2020. “Strain field measurements over 3000 °C using 3D-Digital image correlation.” *Optics and Lasers in Engineering*. 127, 105942.

Rizzolo, S., A. Boukenter, J. Perisse, G. Bouwmans, H. El Hamzaoui, L. Bigot, Y. Ouerdane, M. Cannas, M. Bouazaoui, and J. R. Macé, 2015. “Radiation response of OFDR distributed sensors based on microstructured pure silica optical fibers.” In Proceedings of the 15th European Conference on Radiation and Its Effects on Components and Systems (RADECS), Moscow, Russia, 14–18 September 2015; pp. 1–3.

Sabeur, H., and H. Colina, Effect of heating–cooling cycles on transient creep strain of high performance, high strength and ordinary concrete under service and accidental conditions." *Materials and Structures*. 48; 1561–1579.

Scarella, A., G. Salamone, S. K. Babanajad, A. De Stefano, and F. Ansari, 2017. "Dynamic Brillouin scattering–based condition assessment of cables in cable-stayed bridges." *Journal of Bridge Engineering*. 22, 04016130.

Tan, X., Y. Bao, Q. Zhang, H. Nassif, and G. Chen, 2021. "Strain transfer effect in distributed fiber optic sensors under an arbitrary field." *Automation in Construction*. 124, 103597.

Tang, F., Z. C. Li, Y. Tang, and Y. Chen, H. N. Li, 2020. "Simultaneous measurement of shrinkage and coefficient of thermal expansion of mortar based on EFPI sensors with nanometer resolution." *Measurement: Journal of the International Measurement Confederation*. 152, 107376.

Wang, H., and J. G. Dai, 2019. "Strain transfer analysis of fiber Bragg grating sensor assembled composite structures subjected to thermal loading." *Composites Part B: Engineering*. 162; 303–313.

Webb, G. T., P. J. Vardanega, N. A. Hoult, P. R. A. Fidler, P. J. Bennett, and C. R. Middleton, 2017. "Analysis of fiber-optic strain-monitoring data from a prestressed concrete bridge." *Journal of Bridge Engineering*. 22, 05017002.

Xu, J., Y. Dong, Z. Zhang, S. Li, S. He, and H. Li, 2016. "Full scale strain monitoring of a suspension bridge using high performance distributed fiber optic sensors." *Measurement Science and Technology*. 27, 124017.

Y. Zhu, M. Klegseth, Y. Bao, M. S. Hoehler, L. Choe, G. Chen, 2021. "Distributed fiber optic measurements of strain and temperature in long-span composite floor beams with simple shear connections subject to compartment fires." *Fire Safety Journal*. 121, 103275.

Yang, T., H. Wang, and X. Wang, 2021. "Strain transfer characteristics of multi-layer optical fiber sensors with temperature-dependent properties at low temperature." *Sensors*. 21, 495.

Yao, Y., M. Yan, and Y. Bao, 2021. "Measurement of cable forces for automated monitoring of engineering structures using fiber optic sensors: A review." *Automation in Construction*. 126, 103687.

Ye, C., L. J. Butler, M. Z. E. B. Elshafie, and C. R. Middleton, 2020. "Evaluating prestress losses in a prestressed concrete girder railway bridge using distributed and discrete fibre optic sensors." *Construction and Building Materials*. 247, 118518.

Zhang, L., G. Qiu, G., and Z. Chen, 2021. "Structural health monitoring methods of cables in cable-stayed bridge: A review." *Journal of the International Measurement Confederation*. 168, 108343.

Zhang, S., H. Liu, A. A. S. Coulibaly, and M. J. DeJong, 2021. “Fiber optic sensing of concrete cracking and rebar deformation using several types of cable.” *Structural Control and Health Monitoring*. 28, 1–23.

Zhang, S., H. Liu, J. Cheng, and M. J. DeJong, 2020. “A mechanical model to interpret distributed fiber optic strain measurement at dis-placement discontinuities.” *Structural Health Monitoring*.

Zhou, Z., J. He, G. Chen, and J. Ou, 2009. “A smart steel strand for the evaluation of prestress loss distribution in post-tensioned concrete structures.” *Journal of Intelligent Material Systems and Structures*. 20, 1901–1912.

Zhu, W., Q. Shen, and H. Qin, 2021. “Monitoring of prestress and bond stress of self-sensing FBG steel strand.” *Journal of the International Measurement Confederation*. 177, 109246.

Zhu, Y., and G. Chen, 2022. “Rayleigh scattering based, thermal-induced displacement measurement along a steel plate at high temperature.” *Journal of Infrastructure Intelligence and Resilience*. (accepted)